Università degli Studi di Salerno
Facoltà di Scienze Matematiche Fisiche e Naturali
Dipartimento di Chimica e Biologia

"Development of dosimeters with selective materials to high frequency radiation"

A dissertation submitted in fulfillment of the requirements
for the Degree of Philosophiæ Doctor in
Scienza e Tecnologie per l'Industria Chimica, Farmaceutica e Alimentare
(Indirizzo chimica – XI ciclo)

Candidate:
Dr. Maria Funaro

Supervisor:
Prof. Antonio Proto

Co-Supervisors:
Prof. Paolo Ciambelli

Dr. Patrizia Pelosi

Coordinators:
Prof. Gaetano Guerra

Prof. Paolo Ciambelli

Anno Accademico 2011/2012

Abstract

The clinical use of ionizing radiation to obtain a necrosing or cytotoxic radiobiological effect on tumoral lesions requires wide and complex physical and dosimetrical procedures. In particular, it is necessary to calculate accurately the absorbed dose optimizing its delivery in order to treat the tumor, without affecting the surrounding healthy tissues. Moreover, the technological development of the last few years has led to an evolution in the field of radiotherapy, in the sense of an always bigger conformation of the dose distribution to the volumes to be irradiated, through the use of very complex dose release techniques. For this reason, priority target in radiotherapy is the research and the tuning of suitable systems for dosimetrical measurements. In this context, the research activity presented in this PhD thesis has regarded not only the use and development of conventional dosimeters but mainly the development of new radiation detectors based on nanomaterials. Different nanomaterials have been prepared and tested under photon radiation, such as precursors of silver nanoparticles, manganese doped zinc sulphate nanoparticles, multiwall carbon nanotubes and graphene. This work demonstrates that these nanomaterials, interesting for their fascinating physical and chemical properties, are also very promising to realize dosimeters of new generation.

Dedicated to

Giulia, Alessandra and Fabio

Acknowledgments

I wish to express my sincere gratitude to my supervisor, Prof. Antonio Proto, not only for guiding my first steps in the field of chemistry but above all for his mental opening in taking up new challenges also in a different research field from his own, for his continuous encouragements, for believing in me and for creating a serene work climate.

I am grateful to Dr. Patrizia Pelosi for having introduced me to Radiation Dosimetry and for the technical support during my permanence at Radiotherapy Unit of "G. Rummo" Hospital in Benevento. I had the idea to develop this research project, after speaking with her.

I wish to thank Prof. Paolo Ciambelli for helpful comments and suggestions and for having introduced me to the entrepreneurial world trough the participation to Start Cup Campania 2012, PNI 2012 and Nanochallenge 2012.

I am grateful to Prof. Guerra for his availability for all technical questions concerning the PhD, for useful scientific discussions and advices on patent draft.

I wish to thank Dr. Debora Sarno, Dr. Maria Sarno Dr. Matilde Sublimi for their collaboration; Dr. Fabrizio Bobba, Dr. Antonio Di Bartolomeo and Dr. Nicola Franza for useful discussions and their expert comments.

I am grateful to Dr. Antonio Borsellino, Dr. Anna Colantuoli and Dr Francesco Granata for the use of the LINAC of the Radiotherapy Unit of Check up Diagnostic Center in Salerno and for the technical support.

I wish to thank Dr. Rosario Lanzetta and Dr. Teresa Pironti for the use of the LINAC of the Radioterapy Unit of "G. Rummo" Hospital in Benevento.

Fisciano, 20 Novembre 2012 Maria Funaro

Publications and prizes

The work of this PhD thesis originated the following publications:

- ✓ Funaro M., Di Bartolomeo A., Pelosi P., Saponetti M.S., Proto A. "A dosimeter based on silver-nanoparticle precursors for medical applications with linear response over a wide dynamic range", *Micro & Nano Letters*, 6(9):759-762, 2011;
- ✓ Funaro M., Di Bartolomeo A., Pelosi P., Proto A. "Un rivelatore nanostrutturato sensibile a basse ed alte dosi", *Proceedings VII Congresso Nazionale Associazione Italiana di Fisica Medica*, Catanzaro, 13-16 Settembre 2011;
- ✓ Funaro M., Sarno M., Altavilla C., Proto A., Ciambelli P. "Dosimetro di radiazione "in tempo reale" basato su nanomateriali di carbonio". Patent SA 2012°000011;
- ✓ Funaro M., Boccia M., Granata F., Motta O., Proto A. "A comparison between the accuracy of radiochromic film and 2D arrays in IMRT prostate quality assurance". *Radiologia e Futuro*, 2:266-269, 2012;
- ✓ Funaro M., Sarno M., Ciambelli P., Altavilla C., Proto A. "Real time radiation dosimeters based on vertically aligned Multiwall Carbon Nantotubes and Graphene", Submitted, 2012.

Moreover, the project Sviluppo di dosimetri nanostrutturati (NARRANDO), winner of the first prize both at Start Cup Campania 2012 and PNI 2012 (Life Sciences section), derived from this thesis.

List of Figures

List of Tables

Nomenclature

AC	Alternating Current
AFM	Atomic Force Microscopy
CCVD	Catalytic Chemical Vapor Deposition
CMOS	Complementary Metal Oxide Semiconductor
DC	Direct Current
EBL	Electron Beam Lithography
EBRT/ERT	External Beam Radiation Therapy
EPR	Electron Paramagnetic Resonance
ESR	Electron Spin Resonance
ICRU	International Commission on Radiation Units and Measurements
IMRT	Intensity Modulated Radiation Therapy
IR	Infrared
LINAC	LINear ACcelerator
MOSFET	Metal Oxide Semiconductor Field Effect Transistor
MWCNTs	MultiWall Carbon NanoTubes
NPs	Nanoparticles
PAAm	Poly(allylamine)
PDMS	Polysimethylsiloxane
PMMA	Poly(methyl methacrylate)
PTM	PhotoMultiplier Tube
RF	Radio-Frequency
SEM	Scanning Electron Microscopy

SRS	Stereotaxy Radiosurgey
SBRT	Stereotaxy Body Radiation Therapy
SPRs	Surface Plasmon Resonances
TEM	Transmission Electron Microscopy
TLD	ThermoLuminescence Dosimeter
TPS	Treatment Planning System
UV-Vis	Ultraviolet-Visible
XRD	X-Ray Diffraction
2DXRT	Conventional EXternal beam Radiation Therapy

Measurements Units

eV	Amount of energy gained by the charge of a single electron moved across an electric potential difference of one volt (1 eV= 1.6×10^{-19} joule)
Gy	SI derived unit of the absorbed radiation dose (1 Gy = 1 joule/kg)
Hz	SI unit of frequency, defined as the number of cycles per second of a periodic phenomenon.
keV	1 keV = 10^3 eV
kGy	1 kGy = 10^3 Gy
MeV	1 MeV = 10^6 eV
MHz	1 MHz = 10^6 Hz
MU	Measure of machine output of a LINAC in radiotherapy
torr	Non-SI unit of pressure; 1 torr is approximately equal to 1 mm of mercury.

Table of Contents

INTRODUCTION

The clinical use of ionizing radiation to obtain a necrosing or cytotoxic radiobiological effect on tumoral lesions requires wide and complex physical and dosimetrical procedures. In particular, it is necessary to calculate accurately the absorbed dose optimizing its delivery in order to treat the tumor, without affecting the surrounding healthy tissues. Delivery parameters of a prescribed dose are determined during the treatment planning, which is performed on dedicated computers using specialized treatment planning software. It is crucial to ensure that the prescribed dose is exactly equal to that delivered by the radiation source which is in general a LINear ACcelerator (LINAC).

Over the last few decades, various radiation detectors have been utilized for the measurement of the absorbed dose and in the quality assurance programs, such us ionizing chambers, Fricke dosimeters, radiographic and radiochromic films, thermoluminescence dosimeters (TLDs), semiconductor silicon diodes, Metal Oxide Semiconductor Field Effect Transistor (MOSFET) dosimeters, alanine dosimeters.

The technological development of the last few years has led to an evolution in the field of radiotherapy, in the sense of an always bigger conformation of the dose distribution to the volumes to be irradiated, through the use of very complex dose

release techniques, such as Intensity Modulated Radiation Therapy (IMRT), Stereotactic Radiosurgey (SRS) and Stereotactic Body Radiation Therapy (SBRT). In particular, high gradient of dose are used in IMRT and highly focused beams of ionizing radiation are directed on extremely little lesions in SRS and SBRT.

Priority goal in radiotherapy is the research and the tuning of suitable systems for dosimetrical measurements. In this context, my research activity has regarded the use and development of conventional detectors, such us Fricke dosimeter and radiochromic films and, above all, the development of new dosimetrical systems based on nanomaterials.

In particular, a liquid detector based on precursors of silver (Ag) nanoparticles was developed. The ionizing radiation induces the synthesis of Ag nanoparticles, as it is evident by the color change of the solution from transparent to yellow. The color is due to the establishment of an absorption band in the visible region of the optical spectrum. This band is the result of surface plasmon resonance, i.e. the oscillation of conduction electrons on the metal surface. So, it is possible to understand if nanoparticles are formed not only by color change but also by the presence of an absorption band in the visible region. This allows us to make measurements with an UV-Vis spectrometer. The relation between absorbance peak intensity and absorbed dose is linear over the whole range of doses, from 2 Gy till 120 Gy. Moreover, Atomic Force Microscopy (AFM) shows a correlation between dose and shape/dimension of the radiation-induced nanoparticles.

The response to radiation of other materials, such us silver nanoparticles, precursors of copper (Cu) nanoparticles, precursors of zinc sulphate (ZnS) nanoparticles and manganese (Mn) doped ZnS nanoparticles, was also studied. Among these materials, only Mn doped ZnS nanoparticles show a physical

variation after radiation. In particular, it was found that photoluminescence increases linearly with absorbed dose.

Both the detectors based on Ag nanoparticles precursors and Mn doped ZnS nanoparticles are not absolute dosimeters as ionization chamber or Fricke dosimeter, since they require a calibration before to be used. Ionization chambers are considered the best dosimeters because they allow absolute dose measurements and are characterized by high accuracy, stability over time and reliability. However, they have a relative large physical size which limits their spatial resolution and require a high bias voltage to achieve an acceptable collection of charges, excluding their use for in vivo dosimetry. These disadvantages require the implementation of ionization chambers with improved electrodes. For this reason, real time radiation detectors with electrodes based on vertically aligned Multiwall Carbon Nanotubes (MWCNTs) and Graphene were developed and their charge collection efficiency was studied. Their performance was also compared with that of electrodes made of a conventional material. Moreover, in order to highlight the effect of nanocarbons, reference radiation detectors were also tested. Nanocarbons dosimeters display an excellent linear response to dose and collect more charge than the others at standard bias voltage. In particular, MWCNTs based ionization chamber gives the best charge collection efficiency and it is able to work also to lower bias voltage and zero Volt, allowing in vivo applications. Graphene based ionization chambers show a semiconductor behavior because they have a good charge collection efficiency at standard bias voltage but not at lower Volts. The proposed dosimeters were also patented (Patent SA 2012°000011) and were the subject of the Business Plans presented at Start Cup Campania 2012, PNI 2012 and Nanochallenge 2012.

As further research activity, silver nanoparticles were synthesized by a green method at room temperature, reducing silver nitrate in aqueous solution by

ascorbic acid as reducing agent with the assistance of alanine as capping agent. The silver nanoparticles were characterized by X-Ray Diffraction (XRD), Scanning Electron Microscopy (SEM) and Transmission Electron Microscopy (TEM). The use of alanine in the synthesis influences the shape and the dimensions of nanoparticles. The idea to synthesize silver nanoparticles in alanine stems from the consideration that alanine dosimeters have been introduced on the market and by the successful application of silver nanoparticles precursors as radiation detector. This work can considered preliminary for the construction of a silver/alanine nanocomposites based dosimeters.

The research activity has regarded not only the fabrication of dosimeters but also their exposure to ionizing radiation in order to study their response to dose. For this reason, it was necessary to establish conventions with some Radiotherapy Units. In particular, two conventions were activated respectively with the Radiotherapy Unit of "G. Rummo" Hospital in Benevento and the Radiotherapy Unit of Check up Diagnostic Center in Salerno.

The thesis is structured as follows:

In chapter one the radiation dosimetry fundamentals and the description of standard dosimeters is furnished. Among these, Fricke dosimeter has been reproduced and tested since it is considered the father of chemical dosimeters. Moreover, a characterization of radiochromic films, their calibration and a comparison between their dosimetrical accuracy and that of ionization chambers 2D array was also performed since this dosimeter had been just introduced in the frequented Radiotherapy Unit. This has allowed to gain experience in the field of radiation dosimetry and to take confidence with materials characterization techniques.

In chapter two, the description of a dosimeter based on Ag nanoparticles precursors is furnished and the results of its response to dose, together with AFM

analysis, are discussed. Furthermore, the performance of the proposed dosimeter was compared with that of another detection system based on Ag nanoparticles synthesized in laboratory by chemical reduction instead by radiation.

In chapter three, the syntheses of precursors of copper nanoparticles, precursors of ZnS nanoparticles and Mn doped ZnS nanoparticles are furnished and the response of these materials to radiation is studied.

In chapter four, real time radiation detectors with electrodes based on vertically aligned Multiwall Carbon Nanotubes (MWCNTs) and Graphene are presented. In particular, the synthesis of these nanocarbons, their characterization and their response to radiation is provided.

In chapter five, the synthesis of silver nanoparticles in alanine is presented together with their characterization by XRD, SEM and TEM.

Appendix A contains a detailed description on the working principle of a LINAC and on its components.

In Appendix B, the principal dose release techniques used in Radiotherapy are described.

Appendix C is the Executive Summary of the Business Plan presented for Start Cup Campania competition.

CHAPTER 1
RADIATION DOSIMETRY

Radiotherapy is the process of employing ionizing radiation to eradicate the tumor growth [1, 2]. The goal of radiotherapy is to eradicate tumor cells while sparing surrounding healthy tissue [3]. The sterilization is a result of the radiation interacting with base pairs in the DNA molecule of a cell causing single or double strand breaks.

Radiation dosimetry is a radiotherapy branch. Strictly, it [4] deals with the measurements of the absorbed dose or dose rate resulting form the interaction of ionizing radiation. More broadly, it refers to the determination of these quantities, as well as any of the other radiobiologically relevant quantities, such as kerma, exposure, dose equivalent, energy imparted and so on. One often measures one quantity, usually the absorbed dose and derives another from it through mathematical relationships.

A dosimeter can be defined generally as any device, able to provide the measure of the absorbed dose deposited in its sensitive volume by ionizing radiation. A dosimeter along with its reader is referred to as a dosimetry system.

To function as a radiation dosimeter, the dosimeter must possess at least one physical effect that is a function of the measured dosimetric quantity and can be used for radiation dosimetry with proper calibration. In order to be useful,

radiation dosimeters must exhibit several desirable characteristics such us accuracy and precision, linearity between the dosimetric readings and dose over a wide range, small dose rate dependence, flat energy response, spatial resolution.

Obviously, not all dosimeters can satisfy all characteristics, therefore, the choice of a radiation dosimeter and its reader must be made judiciously, taking into account the requirements of the measurement situation, e.g., in radiotherapy ionization chambers are recommended for beam calibrations (reference dosimetry) and other dosimeters, are suitable for the evaluation of the dose distribution (relative dosimetry) or dose verification. Moreover, the choice of a radiation dosimeter depends on the dose release techniques. In the last years sky-high precision techniques have been introduced such Intensity Modulated Radiation Therapy (IMRT), Stereotaxy Radiosurgey (SRS) and Stereotaxy Body Radiation Therapy (SBRT). In particular, high gradient of dose are used in IMRT and highly focused beams of ionizing radiation are directed on extremely little lesions in SRS and SBRT.

The situation is also more complex if one considers that to ensure that the prescribed dose in the treatment planning is equal to the dose released by the accelerator, the measurement of absorbed dose distribution is performed in a phantom, even if the ultimate check can only be made by *in vivo* absorbed dose measurements. Not all the dosimeters can be used for *in vivo* measurements.

In this chapter, after introducing the principals dosimetrical quantities and describing the properties of a dosimeter, an overview of the most important dosimeters is provided, underlying their advantages and disadvantages. For two of them, the results of some measurements are also discussed. In particular, Fricke dosimeter was reproduced and tested under radiation, since it is considered the father of chemical dosimeters. Moreover, a characterization of radiochromic films, their calibration and a comparison between their dosimetrical accuracy and

that of ionization chambers 2D array was performed since this dosimeter had been just introduced in the frequented Radiotherapy Unit. This has allowed to make experience in the field of radiation dosimetry and to take confidence with materials characterization techniques.

1.1 Definition of absorbed dose and absorbed dose rate

Absorbed dose is defined by ICRU [5] as the expectation value of the energy imparted $(\mathrm{d}\bar{\varepsilon})$ by ionizing radiation to matter of mass $(\mathrm{d}m)$, thus

$$D = \frac{\mathrm{d}\bar{\varepsilon}}{\mathrm{d}m}. \qquad (Eq.\ 1.1)$$

The expectation value of the energy imparted is specified to emphasize that the absorbed dose is a non-stochastic quantity, whereas energy imparted is a stochastic quantity whose value vary discontinuously in space and time.

The mean energy imparted to the matter, $\bar{\varepsilon}$, in a given volume equals the radiant energy, R_{in}, of all those charged and uncharged ionizing particles which enter the volume minus the radiant energy, R_{out}, of all those charge and uncharged ionizing particles which leave the volume, plus the sum, $\sum Q$, of all changes of the rest energy of nuclei and elementary particles which occur in the volume ($Q > 0$: decrease of rest energy; $Q < 0$: increase of rest energy), thus

$$\bar{\varepsilon} = R_{in} - \mathrm{R}_{\mathrm{out}} + \sum Q. \qquad (Eq.\ 1.2)$$

The unit of absorbed dose is Gray (Gy); 1 Gy is equal to 1 Joule (J) per kilograms (kg).

The absorbed dose rate, $\dot{D}$, is the quotient of $\mathrm{d}D$ by $\mathrm{d}t$, where $\mathrm{d}D$ is the increment of absorbed dose in the time interval $\mathrm{d}t$, thus

$$\dot{D} = \frac{\mathrm{d}D}{\mathrm{d}t}. \qquad (Eq.\ 1.3)$$

Its unit is $Gy \cdot s^{-1}$.

1.2 Properties of dosimeters

1.2.1 Precision and accuracy

In radiotherapy dosimetry, the uncertainty associated with the measurement is often expressed in terms of precision and accuracy.

The precision of dosimetry measurements specifies the reproducibility of the measurements and it has to do with random errors due to fluctuations in instrumentals characteristics, ambient conditions, and so on and the stochastic nature of radiation fields. Precision can be estimated from the data obtained in repeated measurements. High precision is associated with a small standard deviation of the distribution of measurement results.

The accuracy of dosimetry measurements expresses the proximity of their expectation value to the "true value" of the measured quantity. Thus, it is impossible to evaluate the accuracy from data themselves, as is done to assess their precision. Accuracy is a measure of the collective effect of the errors in all the parameters that influence the measurements.

Cleary precision and accuracy are separate characteristics. Measurements may be highly precise but inaccurate, or vice versa, or may be strong in both or neither of these virtues.

1.2.2 Linearity

To be useful, a dosimeter must have adequate dose sensitivity throughout the dose range to be measured. A constant dose sensitivity throughout the range provides a linearly proportional between the dosimetric reading and the dose that is desiderable for ease of calibration and interpretation.

However, beyond a certain dose range a non-linearity could set in. The linearity range and the non-linearity behavior depend on the type of dosimeter and its physical characteristics. Three examples of response characteristics of dosimetry systems are sketched in Fig. 1.1. Curve A exhibits linearity over the whole range of dose, curve B first exhibits linearity and then saturation at high doses; curve C first exhibits linearity with dose, then a supralinear behavior, and finally saturation. In general, a non-linear behavior should be corrected for.

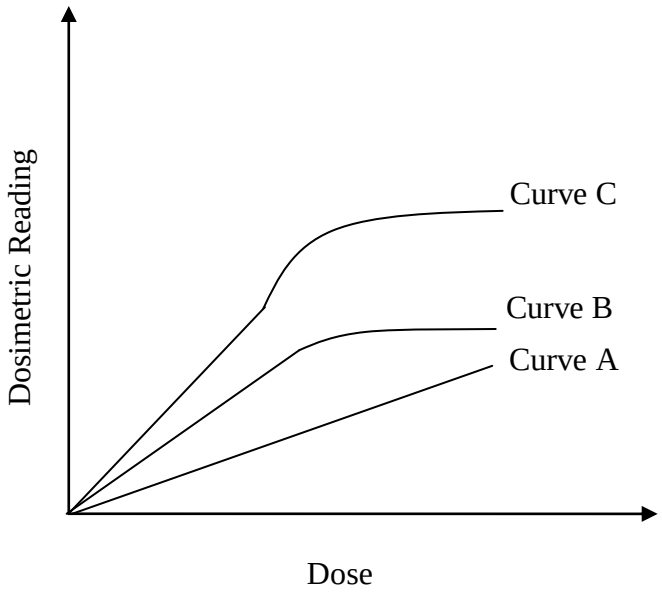

Fig. 1.1: response characteristics of three dosimeters. Curve A first exhibits linearity with dose, curve B first exhibits linearity and then saturation at high doses, curve C first exhibits linearity with dose, then supralinear behavior, and finally saturation.

1.2.3 Dose rate dependence

If a dosimeter is to be used for measuring the time integrated dose (not the dose rate), then it is necessary that its reading is independent on the rate at which the dose is delivered, at least within the range of dose rates to be encountered.

Ideally, the response of a dosimetry system at two different dose rates should remain constant. In reality, dose rate may influence the dosimeter readings and appropriate corrections are necessary.

1.2.4 Energy dependence

The response of a dosimetry system is generally a function of radiation beam quality (energy). Since the dosimetry systems are calibrated at a specified radiation beam quality (or qualities) and used over a much wider energy range, the variation of the response of a dosimetry system with radiation quality (called energy dependence) should be corrected for.

Ideally, the energy response should be flat, i.e., the system calibration should be independent of energy over a certain range of radiation qualities. In reality, the energy correction has to be included in the determination of the dose for most measurement situations.

1.2.5 Spatial resolution and physical size

Because the dose is a point quantity, the dosimeter should allow the determination of the dose from a very small volume, i.e., one need a "point dosimeter" to characterize the dose at a point. The use of dosimeters with very small dimensions, to a great extent, approximates a point measurement.

1.3 Fricke dosimeter

Fricke dosimeter [6, 7] is considered the father of chemical dosimeters. In a chemical dosimeter the absorbed dose is determined from some quantitative change in an appropriate material and any well-characterized chemical reaction may serve as the basis for the dosimeter.

Fricke dosimeter is composed of an aerated solution of 1 mmol/l $Fe(NH_4)_2(SO_4)_2 \cdot 6H_2O$ and 1 mmol/l NaCl in 0.4 mol/l H_2SO_4. Contaminants can significantly affect performance; therefore care must be taken to clean all glassware carefully and to use high purity chemicals. Sodium chloride is added to reduce or eliminate any sensitivity to organic impurities.

The working principle of Fricke dosimeter is based on the oxidation reaction of Fe^{2+} ions to Fe^{3+} ions in consequence of radiation. The ferrous ions are in solution; therefore what is irradiated is mainly water. When ionizing radiation interacting with water, it produces a range of ions, radicals and molecules, such as H, OH, H_2, H_2O_2, H^+, OH^-, e^-_{aq}. Different reaction occurs:

$$\begin{aligned} &H + O_2 \rightarrow HO_2, \\ &Fe^{2+} + HO_2 \rightarrow Fe^{3+} + HO_2^-, \\ &HO_2^- + H^+ \rightarrow H_2O_2, \\ &Fe^{2+} + H_2O_2 \rightarrow Fe^{3+} + OH + OH^-, \\ &Fe^{2+} + OH \rightarrow Fe^{3+} + OH^-. \end{aligned} \qquad (Eq.\ 1.4)$$

Note that the presence of O_2 is necessary.

The average absorbed dose to the Fricke solution, D_S is directly proportional to the change in absorbance, ΔA:

$$D_S = \frac{\Delta A}{\rho l \varepsilon G(Fe^{3+})}, \qquad (Eq.\ 1.5)$$

where ρ is the density of Fricke solution, l is the optical pathlength, ε is the molar linear absorption coefficient for Fe^{3+} ions and $G(Fe^{3+})$ is the number of Fe^{3+} ions formed after the absorption of an energy equal to 100 eV. The molar linear absorption depends on the temperature of the solution during readout; the number of Fe^{3+} ions depends on the temperature during irradiation and also on radiation energy. The absorption peak given in literature is 304 nm.

Fricke dosimeter is classified as an absolute dosimeter. This means that it can measure the absorbed dose deposited in its own sensitive volume without requiring calibration in a known field of radiation. It can be used both for photon and electron radiation source. It satisfies almost all the properties of a dosimeter, except the energy independence. Its limit is the poor response to doses below 4 Gy. Its reading system is very simple being based on an UV measurement. It is not a real time dosimeter since the readout occurs after a timeframe from irradiation.

In order to make experience in the field of radiotherapy and considering its historical importance, Fricke dosimeter was prepared in laboratory and tested under a radiation photon beam, generated by a LINear ACcelerator (LINAC - Precise ELEKTA) of "G. Rummo" Hospital and characterized by a nominal energy of 6 MeV. A vial containing Fricke solution was allocated in a water phantom (PTW) at a source-to-sample distance of 100.0 ± 0.2 cm and irradiated with 5 Gy. The role of the water phantom is to simulate the human body. It essentially consists of a 3D water tank equipped with 3D stainless steel moving mechanism and stepper motors for an accurate detector positioning (Fig. 1.2).

Fig. 1.2: PTW water phantom.

The simulation of the planning treatment for Fricke dosimeter is showed in Fig. 1.3.

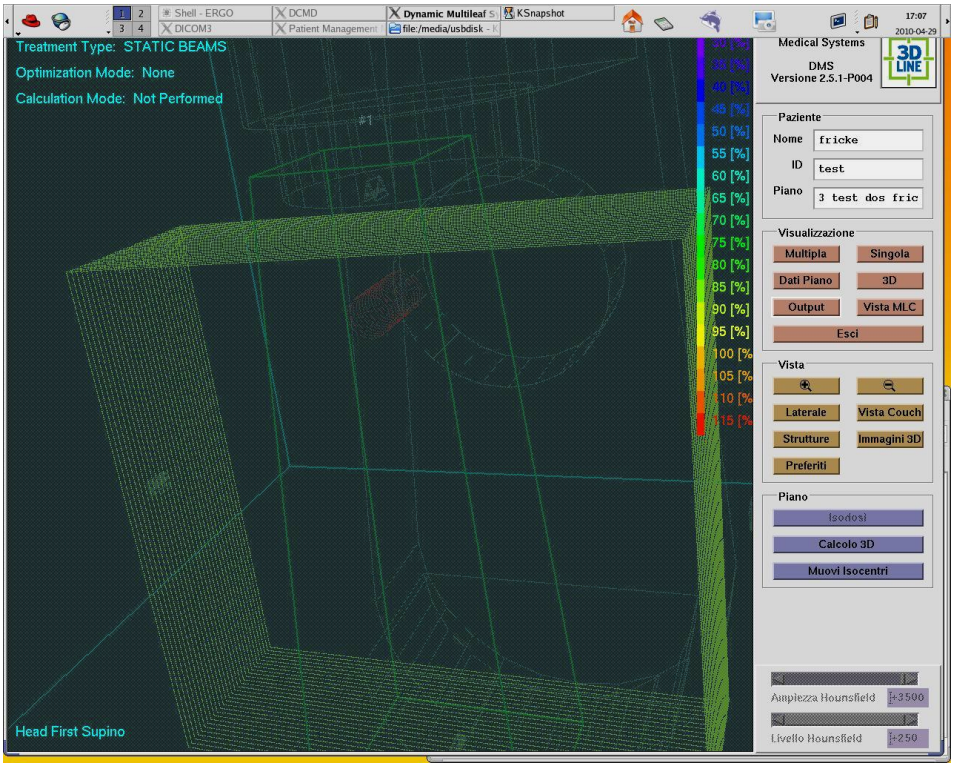

Fig. 1.3: simulation of the treatment planning for Fricke dosimeter with isodose values. In red the cylindrical vial containing the Fricke solution. The color red correspond to a isodose value of 115%.

A change in absorbance occurs after irradiation at a wavelength of 304 nm, as it is evident by the UV-Vis spectrum (Fig. 1.4), measured with a double beam spectrophotometer (PerkinElmer).

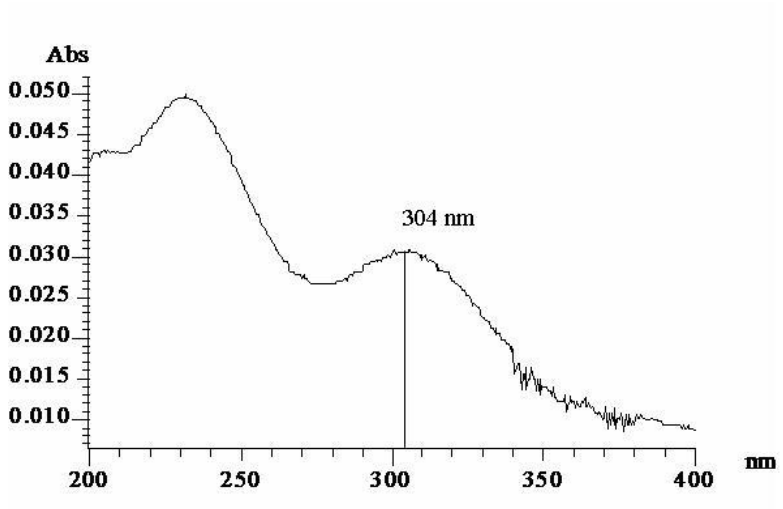

Fig. 1.4: change in absorbance after irradiation vs. wavelength for Fricke solution.

1.4 Ionization chambers

The ionization chamber is the simplest of all gas-filled radiation detectors, and is used for the detection or measurement of ionizing radiation, particularly gamma ray exposure. It basically consists of two metallic plates separated by a distance *D*. The *D* gap is filled with a gas or noble liquid and it defines the sensitive volume of the chamber. A bias voltage is applied to maintain a uniform electric field between the electrodes. When ionizing radiation interacts with the gas or the noble liquid, ion-electron pairs are created. Under the electric field, positive ions and electrons drift in opposite directions toward the anode and cathode, respectively, where the charge produced by ionizing particles is collected.

The ionization chamber is the most widely used type of dosimeter for precise measurements, such as those required in radiotherapy [4]. It is an absolute dosimeter as Fricke detector and, for this reason, it is used for beam calibration.

Ionization chambers have various shapes and sizes depending upon the specific requirements. Two models are essentially used for radiotherapy: thimble chamber and plane-parallel ionization chamber.

A thimble chamber is basically a cavity surrounded by a conductive outer wall and having a central collecting electrode (Fig. 1.5 a). The wall and the collecting electrode are separated with a high quality insulator to reduce the leakage current when a polarizing voltage is applied to the chamber. PTW Farmer Chamber Type 30010 [8] is represented in Fig. 1.5 b.

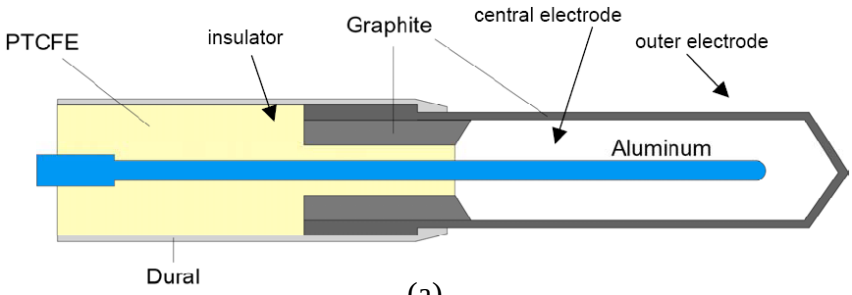

(a)

(b)

Fig. 1.5: (a) basic design of a thimble ionization chamber; (b) PTW Farmer Chamber Type 30010.

A guard electrode is usually provided in the chamber to further reduce the chamber leakage. The guard electrode intercepts the leakage current and allows it to flow to ground bypassing the collecting electrode.

A parallel-plate ionization chamber consists of two plane walls, one serving as an entry window and polarizing electrode and the other as the back wall and collecting electrode as well as guard-ring system. The electrodes usually contain a

several millimeters thick plastic covered with conductive materials, such as aluminum or graphite coated Mylar®.

A schematic diagram of a parallel-plate ionization chamber is provided in Fig. 1.6 a. Advanced Markus Chamber Type 34045 [8] is represented in Fig. 1.6 b.

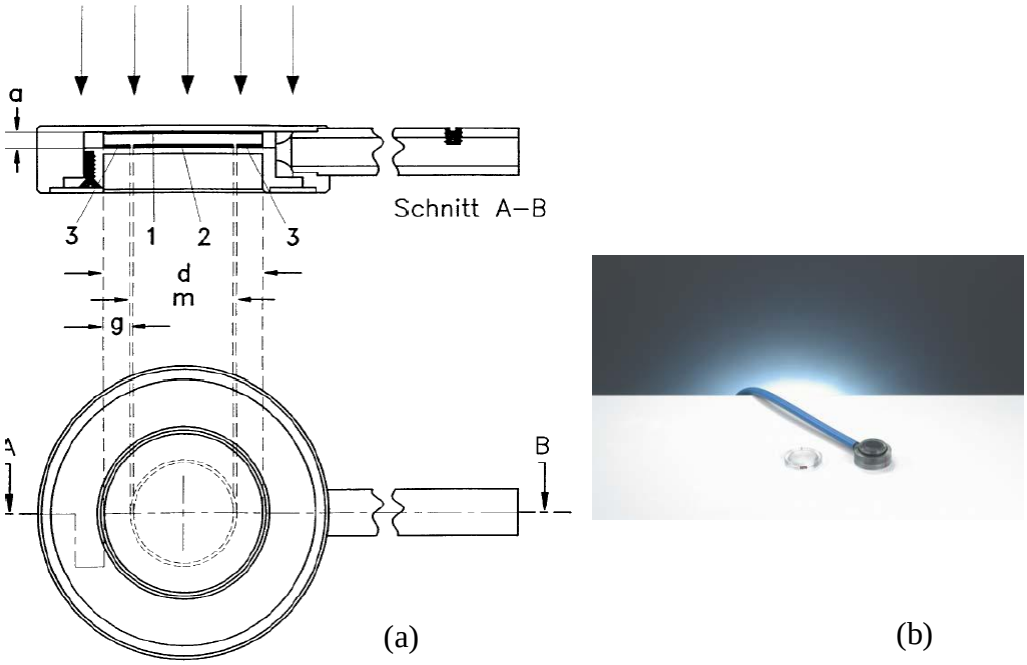

(a) (b)

Fig. 1.6: (a) diagram of a parallel-plate ionization chamber: 1 is the polarizing electrode; 2 is the measuring electrode; 3 is the guard ring; a is the height (electrode separation) of the air cavity; d is the diameter of the polarizing electrode; m is the diameter of the collecting electrode; and g is the width of the guard ring (adapted from the IAEA TRS-381 dosimetry protocol [9]). (b) PTW Advanced Markus Chamber Type 34045.

The reading system consists of an electrometer, i.e. a highly sensitive electronic voltmeter whose input impedance is so high that the current flowing into it can be considered, for most practical purposes, to be zero.

An electrometer used in conjunction with an ionization chamber is a high gain, negative feedback, operational amplifier with a standard resistor or a standard capacitor in the feedback path to measure the chamber current or charge collected over a fixed time interval, as shown schematically in Fig. 1.7.

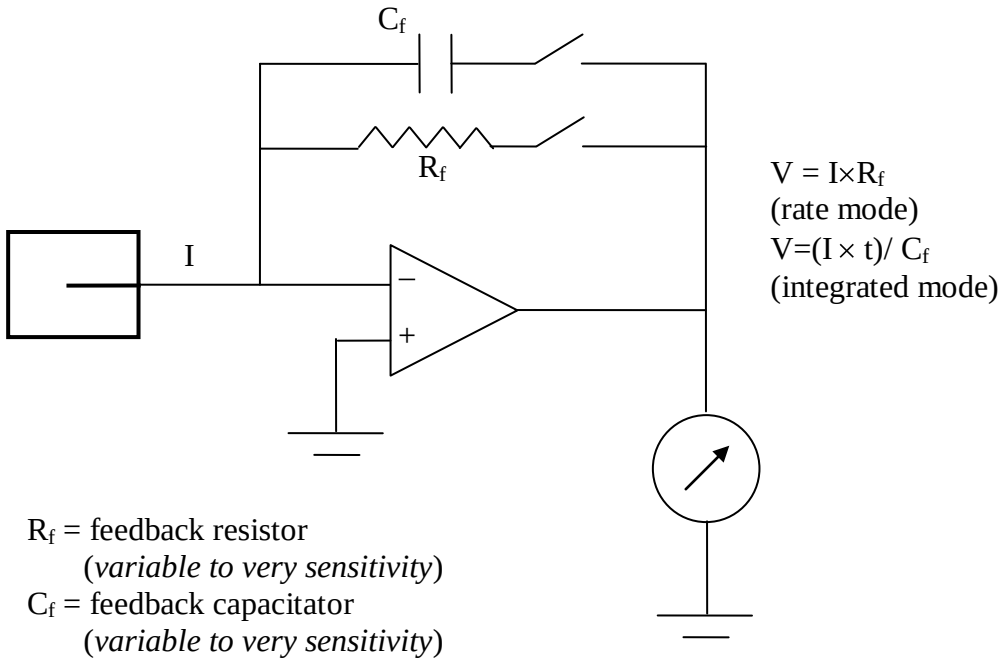

Fig. 1.7: electrometer in feedback mode of operation.

Electrometers are able not only to measure small current of the order of nA or less but also to apply a bias voltage between the electrodes of the ionization chamber. For this reason, they are also equipped with a HV power supply.

Ionization chambers have desiderable properties such as high accuracy, stability over time and reliability. Moreover, they are real-time dosimeter and allow absolute measurements of dose. Ionization chambers present two disadvantages: they have a relative large physical size which limits their spatial resolution and require a high bias voltage to achieve an acceptable collection of charges. This limit excludes their use for in vivo dosimetry.

1.5 Film Dosimeters

1.5.1 Radiographic film

Radiographic film [4, 10] consists of microscopic grains of silver bromide (AgBr), dispersed in a gelatin layer on either one or both sides of a thin plastic base. Incident charged particles produce ion pairs in or near the grains, and their effect is to convert Ag^+ ions to Ag atoms. A few such Ag atoms on a grain (containing typically 10^{10} Ag^+ ions) constitute a latent image, which renders the grain developable by a chemical process. In that process all of the Ag^+ ions are converted to Ag atoms and the bromide is removed, leaving behind an opaque microscopic grain of silver. The presence of this elemental silver may be detected optically and quantitatively related to the absorbed dose.

The radiation effect is measured in terms of the light opacity of the film, as measured by a densitometer, whose principle of operation is shown in Fig. 1.8. Opacity is defined as I_o/I, where I_o is the intensity of light incident on the film, and I is the intensity transmitted through the film. The optical density is defined as $OD = \log_{10}(I_o/I)$ and is a function of dose.

Unexposed film would exhibit a background optical density called the fog density (OD_f). The density due to radiation exposure called the net optical density can be obtained from the measured density by subtracting the fog density.

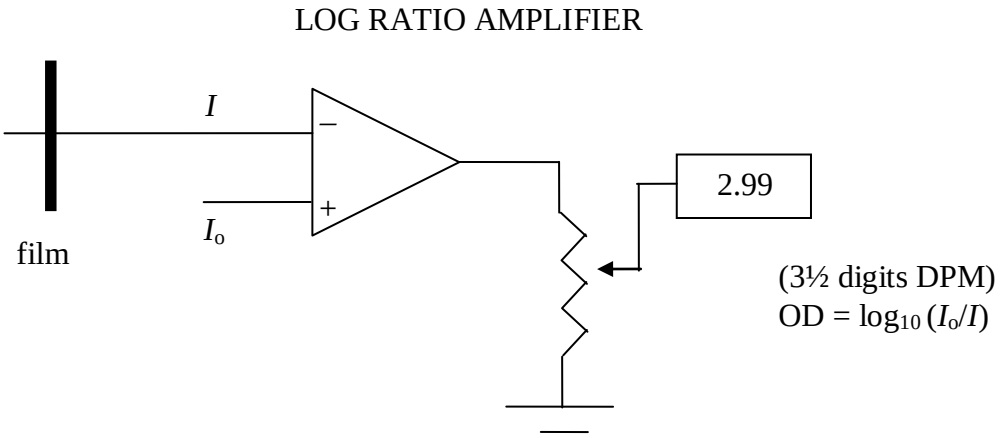

Fig. 1.8: schematic diagram of a basic film densitometer.

The advantage in using radiographic film is that it gives excellent 2D spatial resolution and, in a single exposure, provides information about the spatial distribution of radiation in the area of interest or the attenuation of radiation by objects. However, radiographic film dosimeter presents several disadvantages such as the sensibility to light, a limited useful dose range, the pronounced energy dependence for lower energy photons, the dependence of response on several, difficult to control, parameters and the necessity of a chemical processing. Moreover, the relationship between the dose and OD should be linear, but unfortunately this is not always the case. Some emulsions are linear, some are linear over a limited dose range and others are non-linear.

1.5.2 Radiochromic film

Some of the difficulties encountered with radiographic film are solved with radiochromic film dosimeters. These detectors [10], with very high spatial resolution and relatively low spectral sensitivity variation, are insensitive to visible light, thus offering ease of handling and preparation in room light.

Radiochromic dosimeters color directly and do not require chemical processing; a color change (colorless to blue, red, green, etc.) indicates exposure to radiation. Image formation occurs as a dye-forming or a polymerization process, in which energy is transferred from an energetic photon or particle to the receptive part of the leuko-dye or colorless photomonomer molecule, initiating color formation through chemical changes.

GAFChromic EBT2 film [11] is the radiochromic dosimeter more used. Like its predecessors, this film is self-developing, but has some improved features. In particular it contains a yellow "marker" dye, a feature that minimizes response differences caused by coating anomalies; it is energy independent from 50 keV into the MeV range and is more tolerant to light exposure and less prone to damaged edges when cut.

As reported in [11], GAFChromic EBT2 is made by combining a clear, polyester over-laminate with the active film coating. The substrate of the active film is clear 700 gauge (175 micron) polyester. The substrate is coated with an active layer film, nominally 30 microns thickness, over which a topcoat, nominally 5 microns, is applied. The over-laminate, 200 gauge (50 micron) polyester with approximately 25 microns of pressure-sensitive adhesive, is bonded to the coated side of the active film. The configuration of EBT2 is shown in Fig 1.9 a.

A characterization of GAFChromic EBT2 was performed using the Scanning Electron Microscopy (SEM) of Liquid Crystal Laboratory (LiCryL) at University of Calabria. The identification of the GAFChromic EBT2 layers by SEM is reported in Fig 1.9 b.

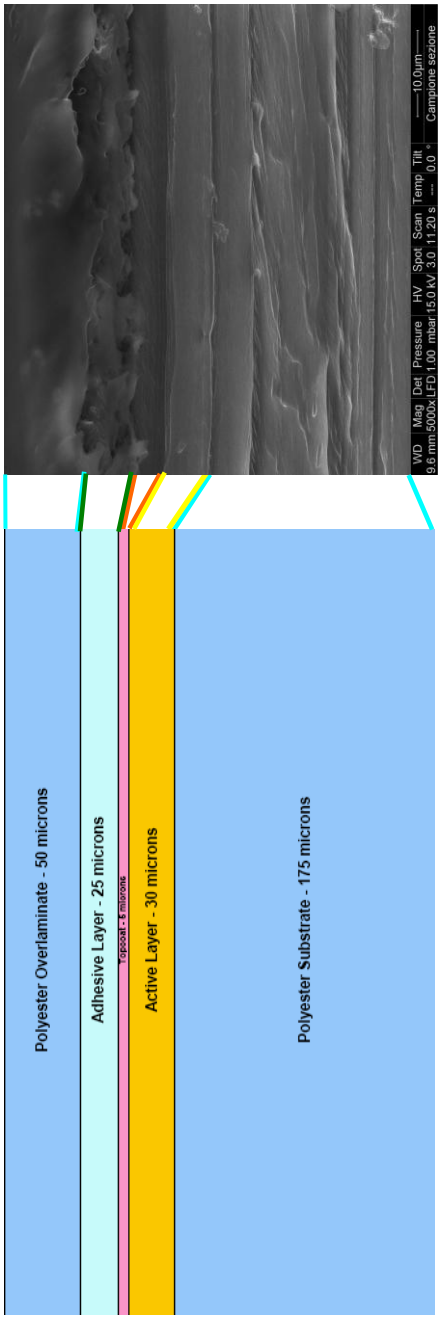

Fig. 1.9: (a) GAFCromic EBT2 configuration; (b) identification of the layers by SEM.

The atomic composition of active layer (Fig. 1.10) was determined by SEM.

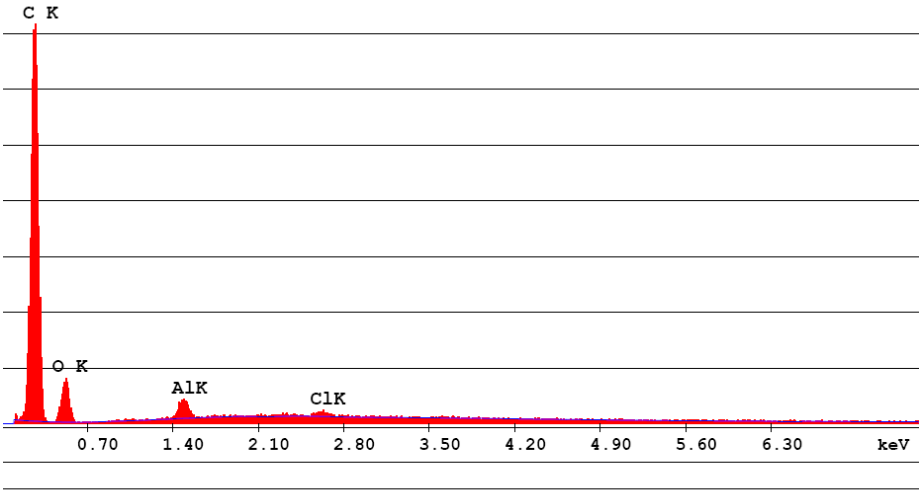

EDAX ZAF Quantification (Standardless)
Element Normalized
SEC Table : Default

Element	Wt %	At %	K-Ratio	Z	A	F
C K	82.83	87.04	0.5749	1.0040	0.6913	1.0001
O K	15.49	12.22	0.0237	0.9873	0.1553	1.0000
AlK	1.28	0.60	0.0094	0.9201	0.8018	1.0001
ClK	0.40	0.14	0.0036	0.8855	1.0216	1.0000
Total	100.00	100.00				

Fig. 1.10: atomic composition of active layer.

The further analysis executed with IR highlights saturation problems due to the fact that films are not completely transparent (Fig. 1.11). However, it is possible to note some peaks in the range 3400-3500 cm^{-1}, probably due to the presence of alcohols, in the range 2950 ~ 2850 cm^{-1} corresponding to the presence of alkanes and in the range 2000 ~ 2500 cm^{-1} (ammine salts).

Even though it has not been possible to determine of what material the film and in particular the active layer were made, the performed measurements have been useful for taking confidence with some characterization techniques.

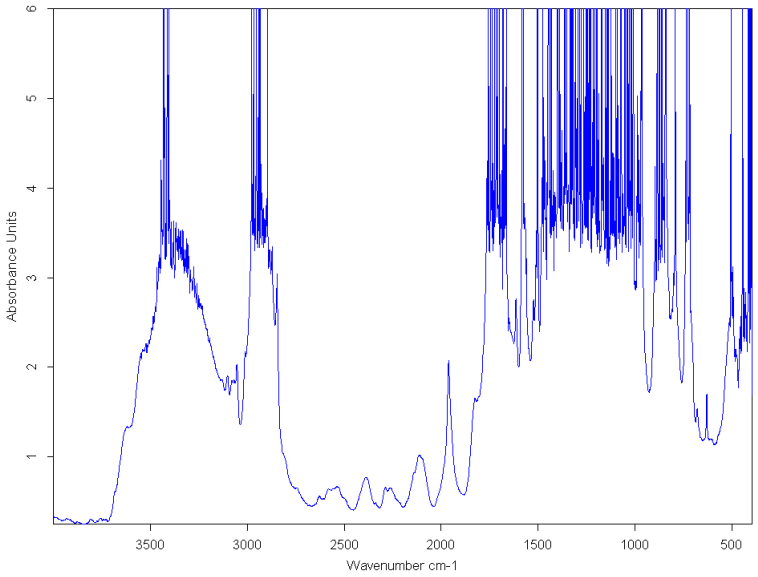

Fig. 1.11: IR spectrum.

1.5.3 Calibration of EBT2 Radiochromic film

A radiochromic film is not an absolute dosimeter so it is necessary to calibrate it before quality assurance programs.

The calibration was performed at Check up Diagnostic Center [12]. Two sheets of GAFChromic EBT2 film were cut to obtain 16 samples. They were appropriately marked to maintain consistent orientation during scanning. In fact it was found that there is a dependence of scanner response on the film orientation upon the scanner plane. The effect is due to the shape and the behavior of the polymers present in the active layer. The active layer films consists of small needle – shaped particles of about 1 – 2μm in diameter and 15 – 25 μm in length which tend to align with their long axis parallel to the direction of the film coverage. This preferential orientation results in a greater spread of light in the direction normal to coverage rather than parallel to it.

Then, each sample was positioned in a phantom according to a set up characterized by the following geometrical parameters: a distance between the

irradiation source and the film equal to 100.0 ± 0.2 cm, a field size of 10 × 10 cm^2 (Fig. 1.12).

Fig. 1.12: the experimental set up used to irradiate radiochromic film GAFChromic EBT2.

The phantom used for experimental measurements is the PTW solid phantom (model 29672) and consists of modules of RW3, a tissue – equivalent material composed by white polystyrene containing 2% of titanium oxide (TiO_2). Other five modules were putted above the film in Fig. 1.12, so that the distance between the source and the surface of the phantom was equal to 95.0 ± 0.2 cm.

The irradiation of the samples was performed using ELEKTA Synergy accelerator with a 6 MeV photon beam. The samples received 5, 20, 40, 60, 80, 100, 120, 140, 160, 180, 200, 250, 300, 350, 400 Monitor Unit (MU), respectively. The MU is the measure of machine output of the LINAC, which is calibrated to give a particular absorbed dose. The conversion factor between Monitor Unit and dose was determined by means of the ionization chamber 30013 Farmer, connected to the electrometer PTW UNIDOS (Fig. 1.13), using the same set up of radiochromic films. In particular 100 MU were given at temperature room equal to (26.8±0.01)°C and pressure of (1008±1)mBar. In this reference setup, 100 monitor units were equal to 92.792 cGy.

Fig. 1.13: ionization chamber 30013 Farmer, connected to the electrometer PTW UNIDOS.

After irradiation, the samples changed color according to the dose (Fig. 1.14).

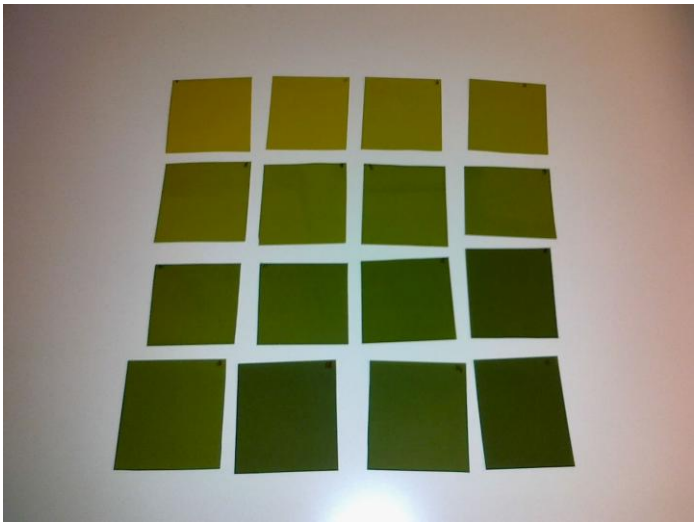

Fig. 1.14: not irradiated sample (up left); the irradiated samples (in total 15) show a different color according to the dose.

The transmission scanner Epson Expression 10000XL, in color mode RGB, 48 bit (16 bits per color), was used as reading system. The scanner was able to detect

transmitted light through the film by adopting a numerical scale, the so called gray levels, ranging from 0 (no transmission) to 65535 (no attenuation).

Before carrying out the several scans of the films, it was necessary to set the various acquisition parameters ensuring that they were always the same in all acquisitions and execute three "empty" scans to ensure the heating of scanner lamp. Each sample was placed in the center of the scanner and it was scanned with 72 dpi resolution and saved as a 48 – bit RGB uncompressed tagged image file format (TIFF) image file.

Then, using ImageJ program, a ROI (Region of Interest) of 4 cm × 4 cm was selected on each sample, avoiding the edges and the average value of the gray levels of the pixels belonging to the ROI (Tab. 1.1) was measured.

Monitor Units (MU)	**Dose (cGy)**	**Mean value of Gray Level <LG>**
0	0	44167
5	4.7	43714
20	18.9	42626
40	37.8	41439
60	56.7	40219
80	75.6	38833
100	94.5	37817
120	113.4	36680
140	132.3	35664
160	151.2	34752
180	170.0	33854
200	188.6	33045
250	236.2	30989
300	283.4	29014
350	330.6	27540
400	377.9	26126

Tab. 1.1: monitor units delivered by the accelerator, corresponding dose values determined by the ionization chamber and mean value of gray levels.

After obtaining these values, it is possible to construct the calibration curve. The best fit between doses and gray – levels was found to be a 2° degree polynomial (Fig. 1.15) [12]:

$$\mathrm{Dose}_{\mathrm{fit}} = a(\mathrm{LG}_{\mathrm{net}})^2 + b(\mathrm{LG}_{\mathrm{net}})$$

with the following parameters:

$$a = 5 \cdot 10^{-7},\ b = 0.0112,\ \mathrm{R}^2 = 0.9994.$$

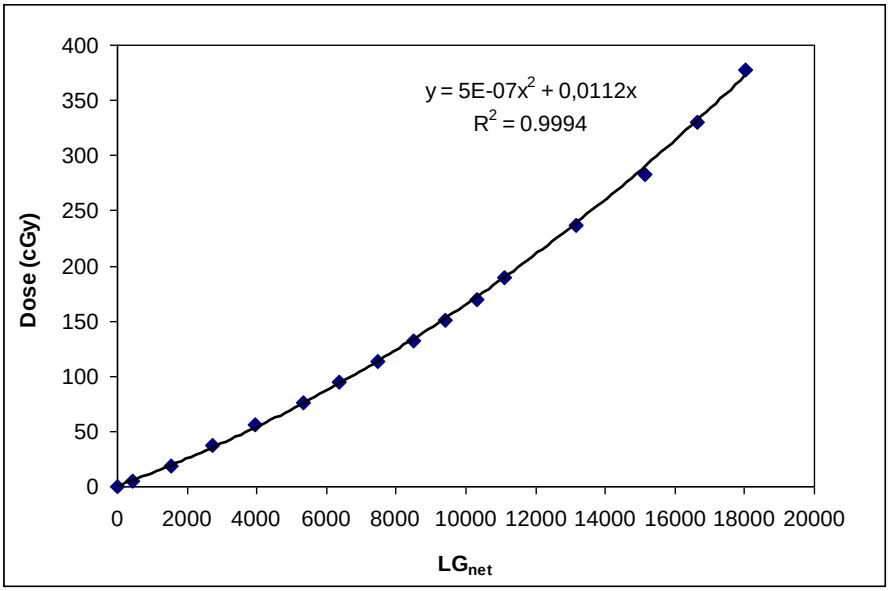

Fig. 1.15: calibration curve of the film EBT2 (Dose vs. LG net).

Despite the advantages of EBT2 radiochromic dosimeters, they do not allow real time real time measurements and they require, as shown, a complex calibration. Moreover, their response in not linear with dose and depends on scanner orientation.

1.5.4 A comparison between the accuracy EBT2 and that of ionization chambers 2D array

After EBT2 film calibration, a comparison between its accuracy and that of an ionization chambers 2D array was performed on an IMRT prostate treatment plane [12].

The 2D array dosimeter used is a matrix of 27 × 27 (729) ionization chambers, which cover an active area of 27 cm × 27 cm (Fig. 1.16). In the 2D array center, there is an ionization chamber which has to be positioned in the beam isocenter. The ionization chambers have cubic shape, size 5 mm × 5 mm × 5 mm with a total volume equal to 0.125cm^3. The sensitive material of chambers is graphite, while the material that surrounds and covers the chambers with a thickness of 5 mm is PMMA. The measurement range of this dosimeter is from 200 mGy to1000 Gy. Although the 2D array is already calibrated in absorbed dose to water, normally each measurement must be corrected for different air pressure and temperature, for the used photon quality and for possible non – water equivalent properties of the phantom. To avoid these corrections, which are time – consuming and susceptible to errors, a simple calibration field with a known dose was applied.

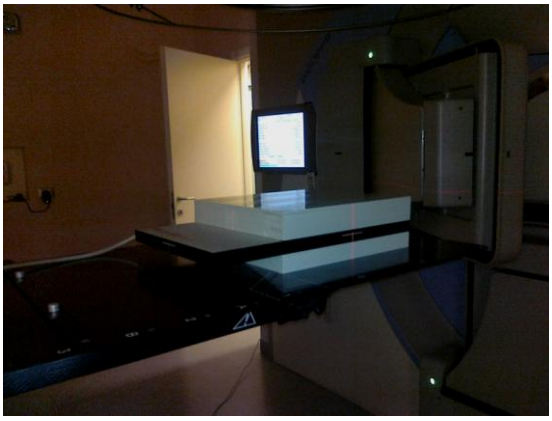

Fig. 1.16: PTW 2D ionization chambers 2D array in solid phantom at a distance between its centre and the beam source equal to 100.0 ± 0.2 cm.

The advantage of using 2D array is that, contrary to single ionization chamber, they allow to acquire planar data in very quick times.

The dosimetric check consists in comparing the dose distribution calculated by the Treatment Planning System (TPS) with that measured by radiochromic film EBT2 or 2D array. TPS calculates the dose in the phantom corresponding to the contribution of each beam which is turned on separately after the dose calculation is finished.

In order to make the comparison, it was necessary to determine the calibration curve through the application FilmCal of PTW Mephysto mc^2 program, for EBT2 film. Then, it was possible to calculate the doses corresponding to the gray levels of the plane treatment on EBT2 film using the calibration curve and the Film Analyze application of PTW Mephysto mc^2 program. After that, the image of the prostate plane tratment with the dose values was saved has .tiff and sent to Verisoft. Finally using the application Compare of Verisoft program in γ index mode [13, 14], the degree of agreement between the calculated dose distribution and that measured by radiochromic film was obtained and resulted about 95% (Fig. 1.17). Both cold and hot spots were present (Fig. 17c).

The application Compare was also used for the quantitative assessment of the agreement between the dose distribution calculated by TPS and that measured with 2D array (Fig. 1.18). The degree of agreement resulted about 94%; cold spots were present (Fig. 1.18 c).

The dosimetrical accuracy of GAFChromic EBT2 film is comparable with that of 2D array. There is not a significant difference in the agreement degree between the dose distribution calculated by TPS and that measured with 2D array and the TPS dose distribution and that measured with GAFChromic EBT2.

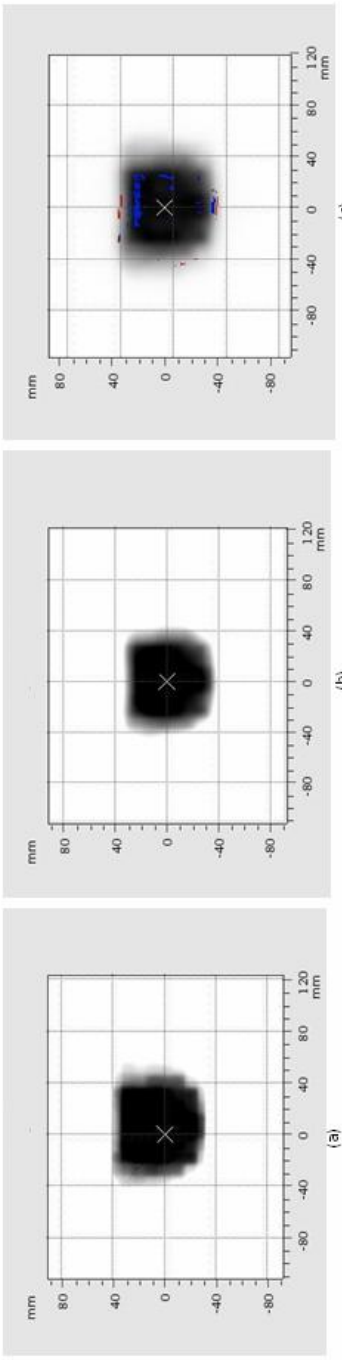

Fig. 1.17: (a) dose distribution measured by radiochromic film, (b) dose distribution calculated by TPS, (c) map of values of γ index.

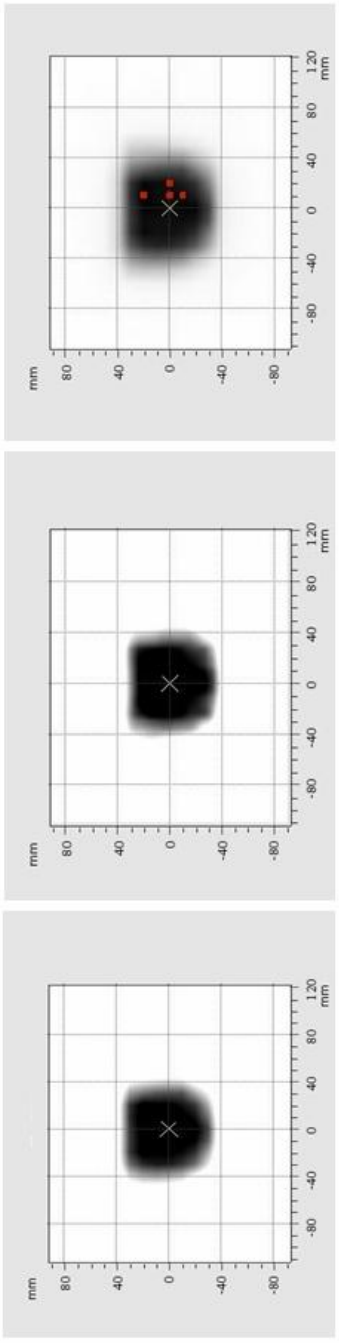

Fig. 1.18: (a) dose distribution measured by ionization chambers 2D array, (b) dose distribution calculated by TPS, (c) map of values of γ index.

Moreover, GAFChromic EBT2 films require an expensive calibration procedure (paragraph 1.5.3), and do not give a real time measurement. On the contrary, 2D arrays are ease to use and do not require an expensive calibration and a delay between irradiation and read – out of the dosimeter. Ion chambers arrays offer the best combination of accuracy, spatial resolution, and ease of use. For this reasons, Malcolm R. McEwen thesis [15], that is better to use ion chamber arrays for IMRT quality assurance, have to be supported.

1.6 Thermoluminescence dosimeters

A thermoluminescence dosimeter (TLD) [4, 16] is a crystalline dielectric material containing suitable activators to make it perform as a thermoluminescent phosphor. The activators provide two kinds of centers, or crystal-lattice imperfections:

- ✓ traps for electrons and "holes", which can capture and hold the charge carriers in an electrical potential for usefully long periods of time;
- ✓ luminescence centers located at either the electron traps or the hole traps, which emit light when the electrons and holes are permitted to recombine at such a centre.

A useful phenomenological model of the thermoluminescence (TL) mechanism is provided in terms of the band model for solids and it can be illustrated with the energy-level diagram, represented in Fig. 1.19. In particular, the left side of this figure shows an ionization event elevating an electron into the conduction band, where it migrates to an electron trap. The hole left behind migrates to a hole trap. At the temperature existing during irradiation, for example room temperature, these traps should be deep enough in terms of potential energy to prevent the escape of the electron or hole for long periods of time, until deliberate heating release either or both of them. In Fig. 1.19 b the effect of such heating is shown.

Assuming that the electron trap in the phosphor is "shallower" than the hole trap, the electron again enters the conduction band and migrates to a hole trap, which can either act as a luminescence centre or to be closely coupled to one. In that case recombination is accompanied by the release of a light photon.

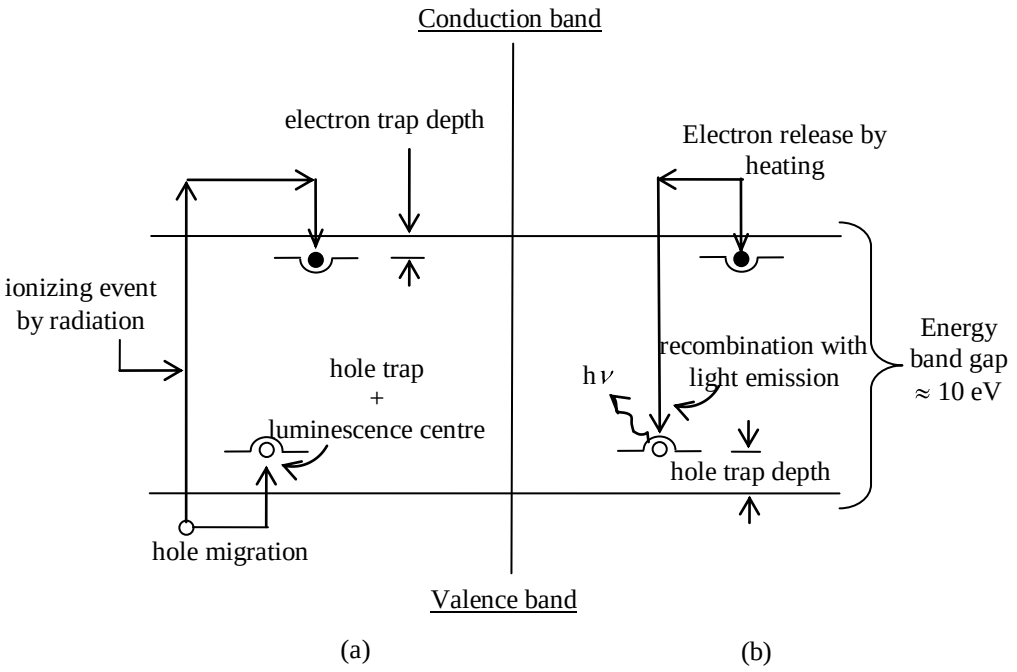

Fig. 1.19: energy-level diagram of the termoluminescence process: (a) ionization by radiation and trapping of electrons and holes; (b) heating to release electrons, allowing luminescence production.

The recombination probability depends on temperature; for this reason, the emission of light is function both of temperature and heating time.

To count the released light which is proportional to trapped electrons and so to the absorbed dose, it is necessary to use photomultiplier tubes. In particular, a basic TLD reading system consists of a planchet for placing and heating the TLD dosimeter; a photomultiplier tube (PMT) to detect the TL light emission, convert

it into an electrical signal, and amplify it; and an electrometer for recording the PMT signal as charge or current. A basic schematic diagram of a TLD reader is shown in Fig. 1.20.

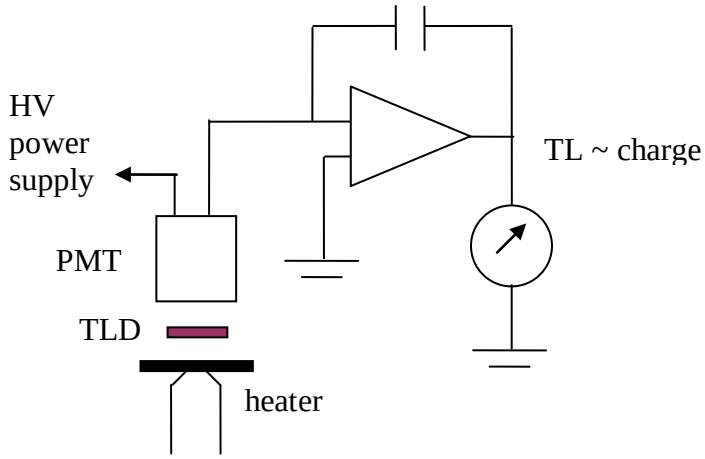

Fig. 1.20: schematic diagram of a TLD reader.

TL dosimeters most commonly used in medical applications are LiF:Mg,Ti, LiF:Mg,Cu,P and $Li_2B_4O_7$:Mn, because of their tissue equivalence. Other TLDs, used because of their high sensitivity, are $CaSO_4$:Dy, Al_2O_3:C and CaF_2:Mn.

TLDs are available in various forms (e.g., powder, chips, rods, ribbon, etc.).

Before they are used, TLDs have to be annealed to erase the residual signal. Well-established reproducible annealing cycles should be used including the heating and cooling rates.

A thermoluminescence dosimeter presents some advantages such as response with a low dependence on photon energy, low cost, small size, the possibility to perform in vivo measurements. Moreover, the dose response is linear over a wide range of doses used in radiotherapy, although it increases in higher dose region exhibiting supralinear behavior before it saturates at even higher doses. The disadvantages include sensitivity to environmental conditions, fading due to

temperature or light effects. Indeed, TL signal decreases in time after the irradiation due to spontaneous emission of light at room temperature. Moreover, TL dosimeters have to be calibrated before they are used (thus they serve as relative dosimeters), require annealing procedures and can not considered real time dosimeter, since the reading time is about 2 min.

1.7 Semiconductor silicon diodes

Semiconductor silicon diode dosimeter [4, 17] is a p-n junction diode. The diodes are produced by taking n-type or p-type silicon and counter-doping the surface to produce the opposite type material.

At the transition from p- to n-type material, a charge-free "depleted region" is formed, over which an electrostatic potential difference of about 0.7 V is created. When ionizing radiation passes through the dosimeter, it produces electron-hole (e-h) pairs. The minority carriers (electrons on the p side and holes on the n side) diffuse into the depleted region. Those carriers within approximately one diffusion length from the junction edge are able to reach it before they recombine. They are then swept across the junction under the action of the electric field due to the intrinsic potential. In this way a current, proportional to the number of charges created, is generated in the reverse direction in the diode and it can be read by an electrometer (Fig. 1.21).

The charge collection in a semiconductor diode is very different than in an ionization chamber. While an ionization chamber requires a high voltage supply, the high electric field across the pn junction makes charge collection possible for the diode without external bias; for this reason they are widely used in routine in-vivo dosimetry on patients. This is not the only advantage. Diodes are more sensitive and smaller in size compared to typical ionization chambers. They are real time dosimeter and exhibit a linear response to dose. The disadvantages

include the dose response dependence on temperature (particularly important for long treatments), on the dose rate and on energy even for small variation in the spectral composition of radiation beams. Moreover, their sensitivity changes with repeated use due to radiation damage; for this reason they are relative dosimeters and require a periodic calibration.

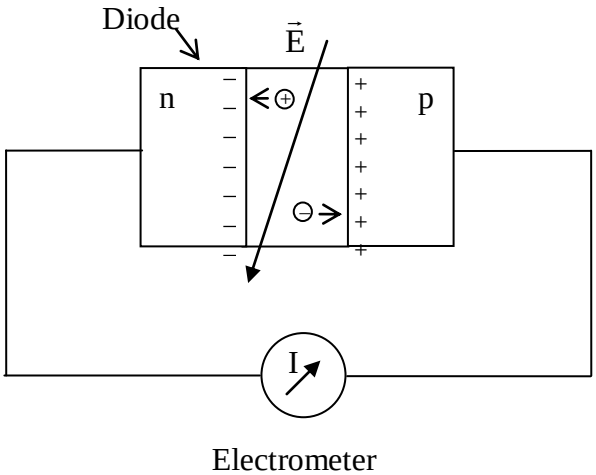

Fig. 1.21: principle of diode detection without external bias (in short-circuit mode).

1.8 MOSFET dosimeters

Like silicon diode dosimeters, Metal Oxide Semiconductor Field Effect Transistor **(**MOSFET**)** dosimeters [18, 19] belong to the category of the semiconductor detectors. The basic MOSFET structure is depicted in Fig. 1.22. The type shown is a p-type MOSFET which is built on a negatively doped silicon substrate (n type). Two terminals of the MOSFET called the source and the drain are situated on the top of a p-doped silicon region. The third terminal shown is the gate. Underneath the gate is an insulating silicon dioxide layer and underneath this

layer is the silicon substrate. The region of the substrate immediately below the oxide layer is known as the channel region.

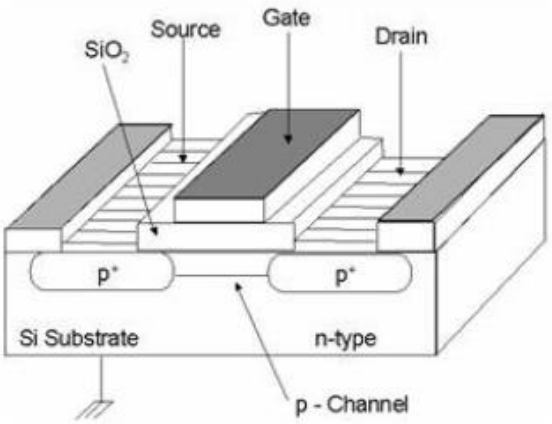

Fig. 1.22: schematic representation of a p-channel MOSFET showing the oxide, the substrate, the source, the drain and the gate.

When a sufficiently large negative voltage is applied to the polysilicon gate a significant number of minority carriers (holes) will be attracted to the oxide/silicon surface from both the bulk silicon substrate and the source and drain regions. Once a sufficient number of holes accumulated there, a conduction channel is formed, allowing the current I_{ds} to flow between source and drain. The voltage necessary to initiate current flow is known as the device threshold voltage (V_{TH}).

When a MOSFET device is irradiated, three things happen within the silicon dioxide layer (sensitive region): a build-up of trapped charge in the oxide; the increase in the number of interface traps; and the increase in the number of bulk oxide traps.

Electron-hole pairs are generated within the silicon dioxide by the incident radiation. Electrons, whose mobility in SiO_2 at room temperature is about 4 orders

of magnitude greater than holes, quickly move out of the gate electrode while holes move in a stochastic fashion towards the Si/SiO_2 interface where they become trapped in long term sites, causing a negative threshold voltage shift (V_{TH}), which can persist for years (Fig. 1.23).

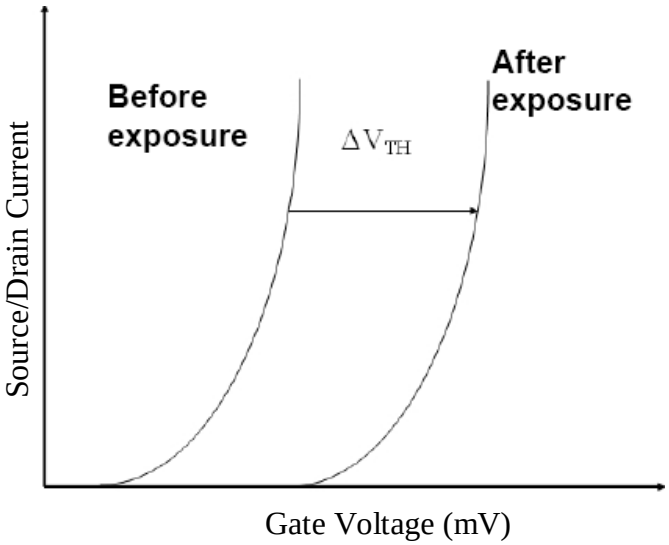

Fig. 1.23: after the irradiation a shift ΔV_{TH} in the drain current versus gate voltage curve is observed.

This voltage shift can then be used for dosimetry. Before and after the irradiation the threshold voltage must be measured. This shift is proportional to the dose.
MOSFET dosimeters advantages are:

- ✓ "immediate" response; however not really "on line" because after termination of the irradiation the gate voltage V_{TH} must be determined;
- ✓ no need for cables to connect the detectors on the patient to an electrometer; however the gate must then be prebiassed before the irradiation;
- ✓ possible use for in vivo measurements;

- ✓ small size of the order of 1 mm^3; this size is smaller than that of diode dosimeters;
- ✓ good reproducibility;
- ✓ non-destructive read-out: possibility of study of dose accumulation over the different treatment sessions, however with a fading correction;
- ✓ response independent on dose-rate.

Their disadvantages are:

- ✓ response dependent on temperature except for dual base dosimeters; their principle consists of associating two detectors with a different grid voltage and of displaying the difference in their signals in order to produce temperature compensated dosimeters;
- ✓ response decrease as a function of accumulated dose, resulting in a limited lifetime of the detector (of the order of 102 Gy in the usual conditions);
- ✓ response dependent on energy: as for diodes, the basic material of a MOSFET is silicon so that a similar energy dependence is observed;
- ✓ slight loss of charge after irradiation: readings to be taken always at the same time delay after termination of the irradiation.

MOSFET dosimeters require a special read-out facility. In the last years, wireless reading system have been developed based allowing to obtain real-time measurements.

1.9 Alanine dosimeters

Alanine, one of the amino acids, pressed in the form of rods or pellets with an inert binding material, is typically used for high dose dosimetry. Alanine dosimeters (Fig. 1.24) can be used at the level of about 10 Gy or more with sufficient precision for radiotherapy dosimetry.

The use of alanine as radiation detectors [20, 21] stems from the fact that the interaction between the ionizing radiation and the alanine molecules produces free radicals. The alanine radical, that is stable at room temperature, is the alanine molecule depleted of the amine group which furnishes an unpaired electron at the central carbon atom. Hence, the concentration of radiation induced free radicals can be measured using an electron paramagnetic resonance (EPR), known also as electron spin resonance (ESR), spectrometer. The intensity is measured as the peak-to-peak height of the central line in the spectrum. The readout is non-destructive.

Fig. 1.24: alanine dosimeters.

Alanine dosimeters present some advantages: they are small, compact, easy to handle and tissue-equivalent. Moreover, they do not require energy correction within the quality range of typical therapeutic beams and exhibit very little fading for many months after irradiation. Their response to dose is linear over a wide range. The disadvantages include the dependence of their response on environmental conditions during irradiation (temperature) and storage (humidity) and a high detection threshold (10 Gy). Moreover, they are not real-time dosimeters.

1.10 Bibliography

[1] Dyk J.V. "The Modern Technology of Radiation Oncology". Medical Physics Publishing, Wisconsin (USA), 1999.

[2] Khan F.M. "The physics of radiation therapy", Lippincott Williams & Wilkins, 2003.

[3] Trevis E.L. "Primer of Medical Radiobiology". Year book Medical Publishers, 1989.

[4] Attix F.H. "Introduction to radiological physics and radiation dosimetry", John Wiley & Sons, 1986.

[5] International Commission on Radiation Units and Measurements, "Radiation Quantities and Units", ICRU Report 33, 1980.

[6] Polvani C. "Elementi di Radioprotezione", Enea, 1996.

[7] Soares C.G., Bright E.L., Ehrlich M. "Fricke dosimeter in high-energy electron beam", National Bureau of Standards Special Publication 250-4, 8754-8761, 1987.

[8] PTW. Catalog Radiation Therapy : detectors available at the web site http://www.ptw.de/1818.html?&no_cache=1&tx_bitptwdwlplus_pi1[collection]=2&tx_bitptwdwlplus_pi1[section]=3

[9] International Atomic Energy Agency (IAEA). "Absorbed dose determination in external beam radiotherapy: An international code of practice for dosimetry based on standards of absorbed dose to water", IAEA Technical Report Series, TRS-398, IAEA, Vienna, Austria (2000).

[10] American Association of Physicists in Medicine Report No. 63. "Radiochromic Film Dosimetry". *Medical Physics* 25(11):2093-2115, 1998.

[11] International Speciality Products. "Gafchromic EBT2, Self-developing film for radiotherapy dosimetry". February 19, 2009.

[12] Funaro M., Boccia M., Granata F., Motta O., Proto A. "A comparison between the accuracy of radiochromic film and 2D arrays in IMRT prostate quality assurance". *Radiologia e Futuro*, 2:266-269, 2012.

[13] Low D., Harms W., Mutic S., Purdy J. "A technique for the quantitative evaluation of dose distributions". *Medical Physics*, 25:656–661, 1998.

[14] Depuydt T, Van Esch A, Huyskens D. "A quantitative evaluation of IMRT dose distributions: refinement and clinical assessment of the gamma evaluation". *Radiotherapy & Oncology*, 62, 309–319, 2002.

[15] Devic S., McEwen M.R., Orton C.G. "Radiochromic film is superior to ion chamber arrays for IMRT quality assurance". *Medical Physics*, 37(3):959–961, 2010.

[16] McKeever S.W., Moscovitich M. "On the advantages and disadvantages of optically stimulated luminescence dosimetry and thermoluminescence dosimetry". *Radiation Protection Dosimetry*, 104(3):263-270, 2003.

[17] Rikner G., Grusell E. "General specifications for silicon semiconductors for use in radiation dosimetry". *Physics in Medicine and Biology*, 32:1109-1117, 1987.

[18] Soubra M., Cygler J. and Mackay G.F. "Evaluation of a Dual Metal Oxide-Silicon Semiconductor Field Effect Transistor Detector as a Radiation Dosimeter". *Medical Physics*, 21 (4):567-72, 1994.

[19] Butson M.J., Rozenfeld A., Mathur J.N., Wong T. P.Y., Metcalfe P.E. "A new radiotherapy surface dose detector: the MOSFET". *Medical Physics*, 23: 655–658, 1996.

[20] Regulla D.F., Deffner U. "Dosimetry by ESR spectroscopy of alanine". *International Journal of Applied of Radiation and Isotopes*, 33: 1101–1114, 1982.

[21] McLaughlin W.L. "ESR dosimetry". *Radiation Protection Dosimetry*, 47(1/4):255-262, 1993.

CHAPTER 2

A DOSIMETER BASED ON SILVER NANOPARTICLE PRECURSORS

In recent years, there has been an increasing interest in Ag nanoparticles for their unique size-dependent optical, electrical, magnetic and antimicrobial properties. Ag nanoparticles have found applications in many fields as catalysis, optics, electronics and nanomedicine [1]. A variety of preparation routes have been proposed for their fabrication, such as chemical reduction [2, 3], microwave dielectric heating [4], sonochemical treatment [5], UV [6] and gamma irradiation [7, 8].

Taking inspiration from the Fricke dosimeter and trying to exploit the unique optical properties of Ag nanoparticles, Šileikaitė et al. have proposed [9] a liquid detector based on precursors of Ag nanoparticles (1mM $AgNO_3$ and 1% $C_6H_5O_7Na_3$ solution), where the ionizing radiation induces the synthesis of Ag nanoparticles, that are then detected by the appearance of a peak around 412 nm in the absorbance spectrum of the colloidal solution.

Part of the research activity was devoted to further develop and study the detector of ref [9]. Two different concentrations of silver nitrate (1mM $AgNO_3$) and sodium citrate (1% and 0.1% $C_6H_5O_7Na_3$) were used as precursors for the formation of Ag nanoparticles in an aqueous colloidal solution. The solutions were exposed to a photon beam varying the absorbed dose in the range from 0.5

Gy to 120 Gy. Photon radiation induces the synthesis of Ag nanoparticles as it is evident by the color change of the solutions and by the presence of a characteristic absorbance peak in the UV spectra. It was found that the device of ref [9] can be optimized by varying the sodium citrate concentration; in particular it is possible to lower the detector working threshold down to 2 Gy by decreasing the sodium citrate concentration to 0.1%. This is an interesting experimental result, since it allows the fabrication of a dosimeter with a wider dynamic range than that of ref [9] and which can be used both in Stereotactic treatments and conventional radiotherapy. In Stereotaxy, a complex and sophisticated technique to irradiate very small lesions, the dose fraction is about 20 Gy, while in conventional radiotherapy treatment the dose fraction is typically 2 Gy. Moreover, a highly linear response between the absorbance peak intensity characteristic of the Ag nanoparticles and the absorbed dose was obtained when the sodium-citrate concentration is lowered. The correlation between dose and shape/dimension of the radiation-induced nanoparticles was also studied by AFM analysis. Furthermore, the performance of the proposed dosimeter was compared with that of another detection system based on Ag nanoparticles synthesized in laboratory by chemical reduction instead by radiation.

In this chapter, the preparation of Ag nanoparticle precursors based detector, its response to radiation and the comparison of its performance with that of a detection system based on Ag nanoparticles are presented [10, 11].

2.1 Materials and Methods

2.1.1 Preparation of silver nanoparticles precursors

Silver nitrate ($AgNO_3$, ACS-ISO, Carlo Erba, IT) and sodium citrate tribasic dihydrate ($C_6H_5O_7Na_3 \cdot 2H_2O$, ACS, Sigma- Aldrich, UK) were used as precursors of Ag nanoparticles. All colloidal solutions of reacting materials were prepared in

distilled water. In a typical sample preparation, 100 ml of a 1mM $AgNO_3$ were heated to boil and then, 2 ml of a 1% $C_6H_5O_7Na_3$ were added drop by drop to the solution, under stirring. Then, the solution was removed from the heating element and cooled down to room temperature under stirring.

The solutions with 1% and 0.1% sodium nitrate concentrations were both prepared by this method.

2.1.2 Irradiation set up

All the samples, each consisting of 4.5 ml of the solution, were exposed to the 6 MeV photon beam generated by the LINAC (Precise Elekta) of "G. Rummo" Hospital in Benevento.

The samples were placed between plastic water sheets (Fig. 2.1) on the central part of the 10×10 cm^2 irradiation field at a source-to-sample distance of 100.0 ± 0.2 cm. They were irradiated at room temperature under atmospheric pressure with exposures corresponding to absorbed doses in the range 0.5 Gy to 120 Gy. The monochromatic photon beam of a radiotherapy LINAC has high homogeneity through the irradiated field respect to the photon beam generated by a ^{60}Co source and used in ref [9].

Fig. 2.1: Linear accelerator (top) and plastic water sheets (bottom).

The calibration of dosimetrical data was implemented on the Treatment Planning System (TPS) of Oncentra – Nuclital to have a correct correlation between the calculated dose 3D-distribution in virtual-patient and real dose absorbed in the irradiated anatomic zone of the patient. In Fig. 2.2 it is showed the sagittal and axial profile of depth-dose for the exposure of 21 Gy for the described experimental set-up.

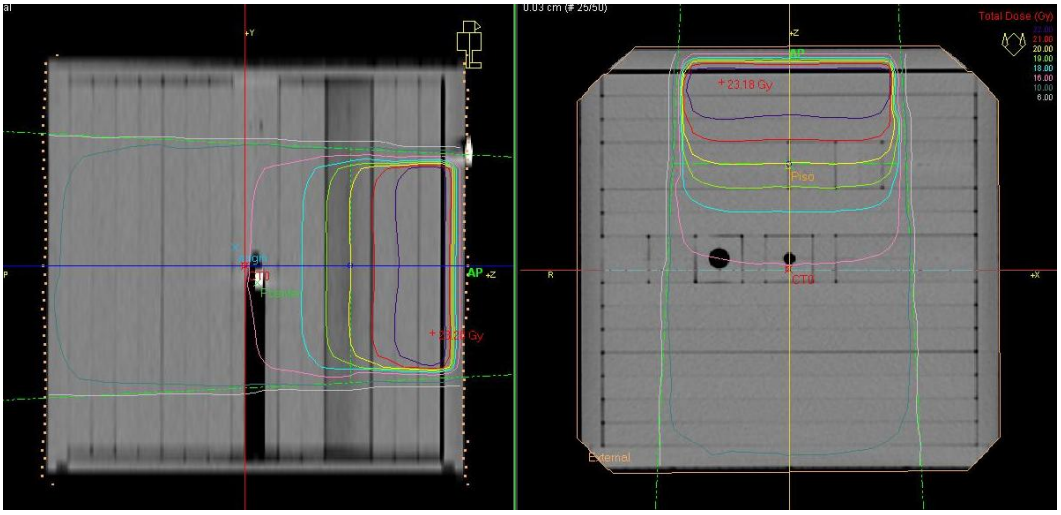

(a) (b)

Fig. 2.2: (a) sagittal and (b) axial profile of depth-dose for the exposure of 21 Gy.

2.1.3 Analysis techniques

The strong interaction of the Ag nanoparticles with light occurs because the conduction electrons on the metal surface oscillate when excited by electromagnetic fields at specific wavelengths. This oscillations, referred to as a surface plasmon resonances (SPRs), result in unusually strong scattering and absorption properties. For this reason, optical absorption spectroscopy is a powerful method to analyze nanoparticles.

The absorbance spectra of our colloidal solutions were measured with a Varian Cary 50 UV-Vis Spectrometer. The shape and the dimensions of the nanoparticles were analyzed by Atomic Force Microscopy (AFM - Multimode Nanoscope V System, VEECO, Santa Barbara, CA) at the laboratory of Scanning Probe Microscopy in Salerno University.

2.2 Results and Discussions

It is well known that when ionizing radiation interacts with aqueous solutions, many radiolytic species are formed: e^-_{aq}, H_3O^+, $H^\bullet$, H_2, H_2O_2, OH^- [7]. The capture cross section of Ag^+ ions from $AgNO_3$ dissolved in water is high; therefore Ag^+ ions are easily reduced to Ag^0 by a hydrate electron e^-_{aq} or by hydrogen atom $H^\bullet$:

$$\begin{aligned} Ag^+ + e^-_{aq} &\rightarrow Ag^0 \\ Ag^+ + H &\rightarrow Ag^0 + H^+ \end{aligned} \quad . \qquad \textit{(Eq. 2.1)}$$

The atoms formed dimerize and progressively coalesce into larger clusters, producing silver nanoparticles:

$$\begin{aligned} Ag^0 + Ag^0 &\rightarrow Ag_2 \\ Ag^0 + Ag^+ &\rightarrow Ag_2^+ \\ Ag_n + Ag^+ &\rightarrow Ag_{n+1}^+ \\ Ag_{n+1}^+ + e^-_{aq} &\rightarrow Ag_{n+1} \end{aligned} \quad . \qquad \textit{(Eq. 2.2)}$$

2.2.1 Dosimeter based on colloid of precursors with 1% sodium citrate

The dosimeter constituted by a colloidal solution with 1mM $AgNO_3$ and 1% $C_6H_5O_7Na_3$ was irradiated at several doses in the range 0.5 Gy - 120 Gy. It was observed that the colloid, originally transparent, changes color becoming yellower

for increasing dose (compare Fig. 2.3 a and Fig. 2.3 b). The change in color suggests that Ag nanoparticles are formed. This is confirmed by UV analysis.

(a) (b)

Fig. 2.3 hole containing the sample in the plastic water sheets (a) before and (b) after (21Gy) irradiation.

Indeed, the absorbance spectra of irradiated samples show the formation of a peak slightly above 420 nm, characteristic of Ag nanoparticles (Fig. 2.4); such peak is not present in the unexposed samples, thus confirming the irradiation-induced formation of nanoparticles. The intensity of the peak increases with the dose and is clear already at 8 Gy. Differently from ref [7] and [8], where doses of the order of a kGy are used to produce Ag nanoparticles, we find, in agreement with ref [9], that doses of some Gy are already sufficient for this process.

The peak intensity shows a rough linear dependance on the absorbed dose as shown in Fig. 2.5.

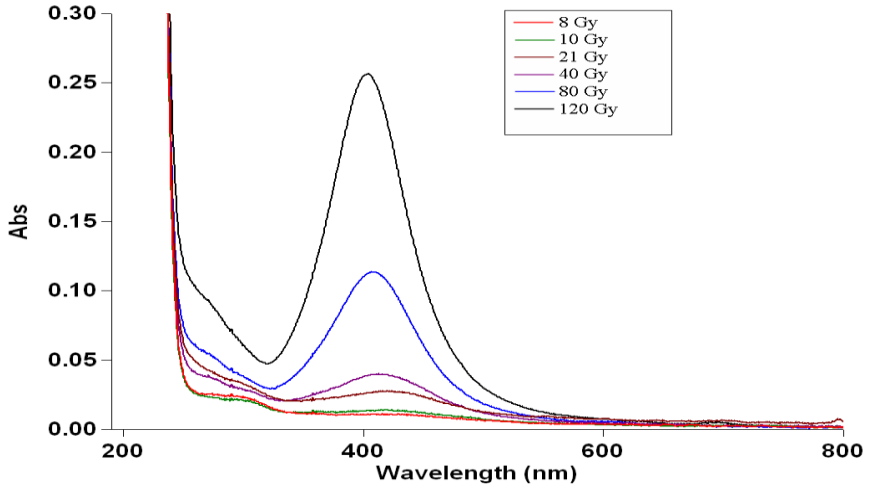

Fig. 2.4: absorbance spectra of colloidal solutions with 1mM $AgNO_3$ and 1% $C_6H_5O_7Na_3$ after gamma irradiation at 8 Gy, 10 Gy, 21 Gy, 40 Gy, 80 Gy, 120 Gy respectively.

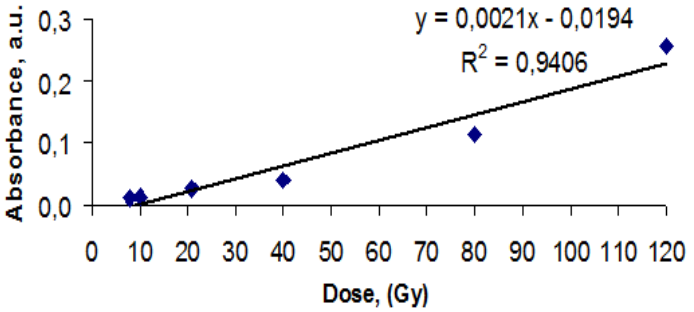

Fig. 2.5: dependence of the absorbance peak intensity on the absorbed dose.

2.2.2 Dosimeter based on colloid of precursors with 0.1% sodium citrate

The dosimeter based on colloid with 1mM $AgNO_3$ and 0.1% $C_6H_5O_7Na_3$ has remarkable properties and advantages with respect to the previous one. The peak in the absorbance spectrum, corresponding to Ag nanoparticles, is evident already at 2 Gy (Fig. 2.6). This proves that the working threshold of the detector can be

controlled by the concentration of sodium citrate, and can be lowered below 2 Gy for reduced $C_6H_5O_7Na_3$ concentrations.

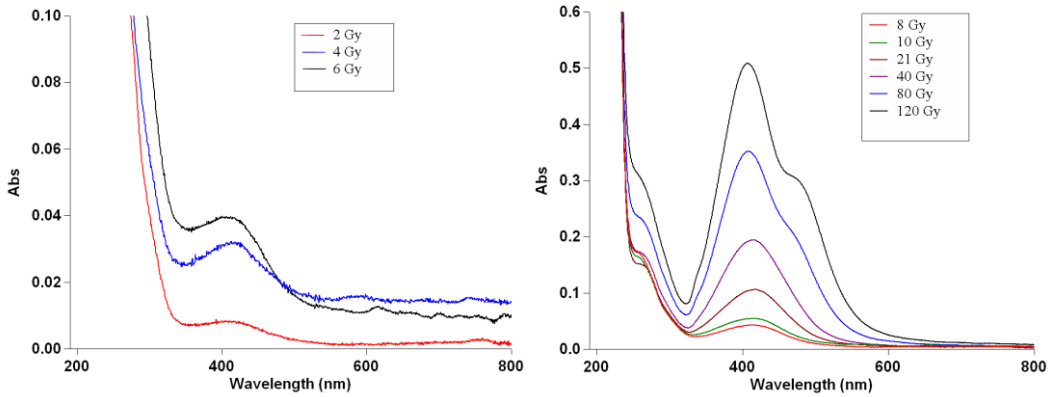

(a) (b)

Fig 2.6: absorbance spectra of colloidal solution with 1 mM $AgNO_3$ and 0.1% $C_6H_5O_7Na_3$ after gamma irradiation with 2 Gy, 4 Gy, 6 Gy (a) and 8 Gy, 10 Gy, 21 Gy, 40 Gy, 80 Gy, 120 Gy (b).

Remarkably the relation between absorbance peak intensity and absorbed dose becomes highly linear (Fig. 2.7) over the whole range of doses, from 2 Gy till 120 Gy. The steeper fitting line indicates to a more sensitive detector. The lower dose sensitivity, the linear and steeper behavior obviously make the detector with reduced sodium citrate concentration better than the one with 1% $C_6H_5O_7Na_3$.

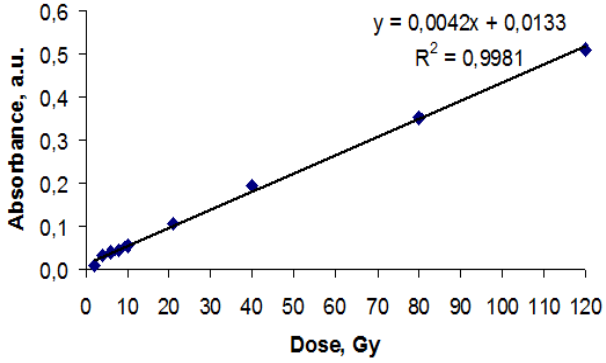

Fig: 2.7: dependence of the absorbance peak intensity on the absorbed dose.

For both detectors that have been described, it was also checked that the nanoparticles synthesized by photon radiation are stable over a period of 5 days. There is no need to test over a longer period for our dosimetric purposes.

The proposed detector belongs to the class of relative dosimeters which can be used for quality assurance programs and not for the calibration of radiation beams.

2.2.3 AFM analysis

An AFM analysis was also performed on the 0.1% $C_6H_5O_7Na_3$ samples irradiated at 8 Gy and 21 Gy respectively. Droplet-evaporation method was used for preparing AFM samples from liquid suspensions. A droplet of liquid was deposited on freshly cleaved mica and it was waited its evaporation to allowing the sample sitting.

It was found that the nanoparticles synthesized at 8 Gy are smaller than those synthesized at 21 Gy, which tend to have a more elongated shape (Fig. 2.8): nanoparticles produced at 21 Gy are 4-5 times wider and longer that those produced at 8 Gy and present a higher length-to-width ratio; longer particles likely corresponding to the beginning of nanorod formation. This confirms ref [9] which suggests that Ag nanorods can be formed at higher doses and ref [6] that shows evidence of two species, Ag spherical nanoparticles and Ag nanorods, when the solution is irradiated for longer times. The absorption spectra of larger metallic colloidal suspensions can show broader or additional peaks in the UV range due to the excitation of further plasma resonances or higher multipole plasmons [12]. The presence of the bump at ~ 470 nm and at ~ 460 nm on the peak at 407 nm in the absorption spectra of the colloids exposed to 120 Gy and 80 Gy (Fig. 3b) is a further evidence of the formation of more elongated nanoparticles.

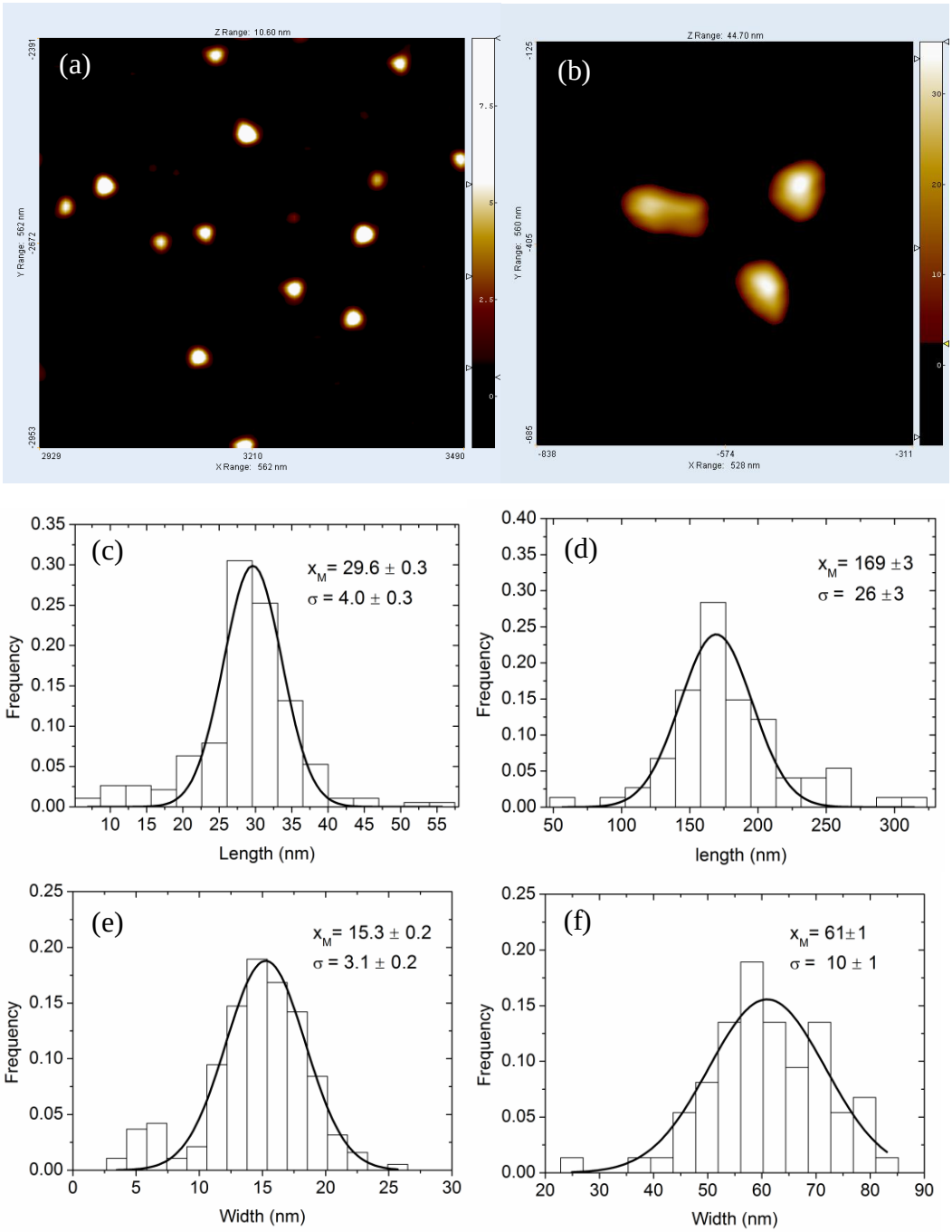

Fig. 2.8: AFM image of the nanoparticles synthesized by 8 Gy (a) and 21 Gy (b). Length and width distributions of the nanoparticles synthesized by 8 Gy (c)-(e) and by 21 Gy (d)-(f), respectively.

2.3 A comparison with a dosimeter based on colloid of Ag nanoparticles synthesized by chemical reduction

The performance of the dosimeter described in section was also compared with that of a detector based on silver nanoparticles synthesized by the chemical reduction reported in [13]. In this paper, the formation kinetics of silver nanoparticles during synthesis of silver colloidal solution (silver nitrate reduction with sodium citrate) was investigated. To prepare silver nanoparticles, 100 ml of 1 m M $AgNO_3$ was heated to boiling. To this solution 1 ml of 1 % trisodium citrate was added drop by drop. During the process solution was mixed vigorously. The absorption spectra were taken after different times from boiling to find when the formation of silver nanoparticles starts. After 20 min of boiling, a small absorption band around 400 nm was observed [13]: this is an evidence of nanoparticles formation.

Silver nanoparticles were synthesized with the above procedure with the only difference that 0.1 % sodium citrate concentration was used. The nanoparticles start to form after a shorter time of above 10 min using the lower concentration. Note that, for nanoparticles synthesized by radiation, lower doses were necessary to synthesize the precursors when 0.1 % sodium citrate concentration was used. So, nanoparticles start to form in less time or at a smaller dose with a lower sodium citrate concentration.

The silver nanoparticles were irradiated with doses in the range from 0.5 Gy to 120 Gy, using the same experimental set-up of section 2.1.2. In this case, it was not found absorption peak intensity enough to build a detector over the explored range of doses, as shown in Fig. 2.9.

This demonstrated that to realize a working dosimeter it is much better to use precursors of Ag nanoparticles instead of nanoparticles already synthesized.

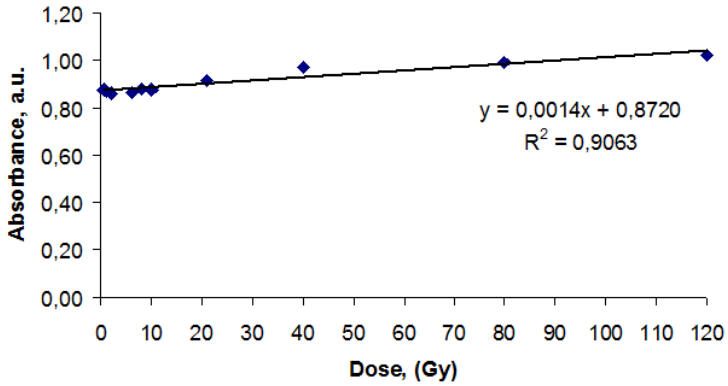

Fig. 2.9: dependence of the absorbance peak intensity on the absorbed dose for Ag nanoparticles synthesized by chemical reduction.

2.4 Bibliography

[1] Peres D.P. "Silver nanoparticles". In-The, 2010.

[2] Šileikaitė A., Prosyčevas I., Puišo J., Juraitis A., Guobienė A. "Analysis of Silver Nanoparticles Produced by Chemical Reduction of Silver Salt Solution". *Materials Science* (*Medžiagotyra*), 12(4):287 – 291, 2006.

[3] Guzmán M.G., Dille J., Godet S. "Synthesis of silver nanoparticles by chemical reduction method and their antibacterial activity". *World Academy of Science, Engineering and Technology*, 43:357 – 364, 2008.

[4] Patel K., Kapoor S., Dave D.P., Mukherjee T. "Synthesis of Nanosized Silver Colloids by Microwave Dielectric Heating". *J. Chem. Sci.*, 117(1):53 – 60, 2005.

[5] Mănoiu V. S., Aloman A. "Obtaining silver nanoparticles by sonochemical methods". *U.P.B. Sci. Bull., Series B*, 72(2):179 – 186, 2010.

[6] Szymańska-Chargot M., Gruszecka A., Smolira A., Bederski K., Głuch K., Cytawa J., Michalak L. "Formation of nanoparticles and nanorods via UV irradiation of $AgNO_3$ solutions". *Journal of Alloys and Compounds*, 486(1-2):66-69, 2009.

[7] Temgire M.K., Joshi S.S. "Optical and structural studies of silver nanoparticles". *Radiation Physics and Chemistry* , 71:1039 – 1044, 2004.

[8] Gasaymeh S.S., Radiman S., Heng L.Y., Saion E., Saeed G.H.M. "Synthesis and Characterization of Silver/Polyvinilpirrolidone (Ag/PVP) Nanoparticles Using Gamma Irradiation Techniques". *American Journal of Applied Sciences*, **7**(7):892 – 901, 2010.

[9] Puišo J., Laurikaitienė J., Adlienė D. and Prosyševas I. "Liquid radiation detectors based on silver surface plasmon resonance phenomena". *Radiation Protection Dosimetry*, 139(1-3):353–356, 2010.

[10] Funaro M., Di Bartolomeo A., Pelosi P., Saponetti M.S., Proto A. "A dosimeter based on silver-nanoparticle precursors for medical applications with linear response over a wide dynamic range". *Micro & Nano Letters*, 6(9): 759-762, 2011.

[11] Funaro M., Di Bartolomeo A., Pelosi P., Proto A. "Un rivelatore nanostrutturato sensibile a basse ed alte dosi", *Proceedings VII Congresso Nazionale Associazione Italiana di Fisica Medica*, Catanzaro, 13-16 Settembre 2011.

[12] Wang D., Song C., Hu Z., Zhou X. "Synthesis of silver nanoparticles with flake-like shapes". *Materials Letters*, 59(14-15):1760-1763, 2005.

[13] Šileikaitė A., Puišo J., Prosyševas I., Tamulevičius S., "Investigation of Silver Nanoparticles Formation Kinetics During Reduction of Silver Nitrate with Sodium Citrate". *Materials Science (Medžiagotyra)*, 15(1):21 – 27, 2009.

CHAPTER 3
RESPONSE TO RADIATION OF CU AND ZNS NANOPARTICLES

The results obtained in Chapter 2, where a radiation dosimeter based on precursors of Ag nanoparticles is presented, led to ask us what could happen if elements belonging to the same group of Ag were used as precursors of nanoparticles and exposed to radiation. The choice was on copper (Cu), because it is cheaper than Ag. Unfortunately, the results were not as hoped, probably because a copper salt with an oxidation state equal to +2 was used in the synthesis. Another reason could be the use of a polymer as capping agent, which reduces the mobility of copper ions. This could require higher doses than used, making the system not suitable for dosimetrical purposes.

Since the wished results were not obtained, it was decided to focus the attention on semiconductor nanoparticles. Indeed, in recent years, there has been a considerable interest on these nanoparticles, because of their unique electronic and chemical properties, such as large surface-to-volume ratio and confinement of electronic states [1, 2]. As an example, the electronic band gap in semiconductor nanoparticles is directly related to the size of the nanoparticle, allowing size-driven control over properties, such as conductance and emission wavelength [2, 3]. The versatility of physical and chemical properties makes semiconductor

nanoparticles promising for applications in different fields, ranging from optoelectronics [3] and sensing [4] to catalysis and biomedicine [5].

Among semiconductors, ZnS is a commercially important II–VI semiconductor having a wide optical band gap, rendering it a very attractive material for optical applications especially in nanocrystalline form.

In order to construct a radiation dosimeter, two strategies were followed. ZnS nanoparticles precursors were first prepared to understand if their synthesis could occur by gamma radiation, as for Ag nanoparticles precursors. This approach has not led to the wished result, probably because the doses used were too low and the precursors was not dispersed in an aqueous system but polystyrene films, containing the precursors, were prepared. As second approach, instead to synthesize precursors, nanoparticles were prepared directly in laboratory and possible chemical/physical changes after radiation were studied. In particular, Mn doped ZnS nanoparticles were synthesized, dissolved in glycerin and exposed to radiation. Photoluminescence spectra were analyzed both for irradiated and not exposed samples. It was found a linear dependance between the photoluminescence intensity and the absorbed dose. These results are very promising for the construction of a relative dosimeter.

In this chapter, the syntheses of precursor of Cu nanoparticles, ZnS nanoparticles precursors and Mn doped ZnS nanoparticles are described and their response to radiation is discussed.

3.1 Cu nanoparticles precursors

Since the success obtained in the formation of silver nanoparticles by water radiolysis due to gamma radiation, which allowed an application in the field of dosimetry (see chapter 2), it was also our aim to check what could happen if elements belonging to the same group of Ag were used as precursors of

nanoparticles and exposed to radiation. The choice was on copper (Cu) because it is cheaper than Ag.

In ref [6] copper nanoparticles are synthesized by a simple chemical reaction, based on the reduction of copper(II) salt with hydrazine in aqueous solution under atmospheric air in the presence of poly(allylamine) (PAAm) capping agent. The advantages of this synthetic method include the production of water dispersible copper nanoparticles, with reasonably uniform size and relatively higher yield, at room temperature under no inert atmosphere, making the synthesis more environmentally friendly.

In a typical synthesis, 0.5 ml of a 0.1 M copper sulphate ($CuSO_4$) solution and 0.22 ml of PAAm were completely dissolved in 10 ml of Millipore H_2O, under vigorous stirring at 60 °C for 20 min, forming a transparent light-blue solution (Fig. 3.1). Then, 0.7 ml of a 0.5 M sodium hydroxide (NaOH) solution was added dropwise into the above solution, forming a greenish solution. After stirring for 20 min, 1.0 mmol of hydrazine (N_2H_4 $3H_2O$) solution was dropped into the above solution under constant stirring. The resulting solution was kept in a water bath at 60 °C and it become first light yellow ad then red, after the adding of N_2H_4 $3H_2O$.

Fig. 3.1: schematic illustration of the procedure used for copper nanoparticles formation [6].

The growth of colloidal Cu nanoparticles during the reaction went through several steps as observed from a set of color changes, from light yellow to wine red (Fig. 3.6). In particular, after 30 min of reaction, a yellow solution, which displayed a very weak absorption peak at 578 nm corresponding to the plasmon resonance of Cu_2O nanoparticles, was observed. However, after 40 min of overall reaction time, the solution turned red and showed a well-defined absorbance band at ~560 nm, corresponding to the plasmon resonance of Cu nanoparticles [6].

With the aim to check if ionizing radiation could be responsible of copper nanoparticles formation by water radiolysis, both the blue-light and the greenish solution was exposed to a the 6 MeV photon beam generated by the LINAC (ELEKTA Synergy) of Check up Diagnostic Center. The experimental irradiation set up was equal to that used for radiochromic film of paragraph 1.5.3 and for Ag nanoparticle precursors based detector of Chapter 2: the samples were placed at the centre of a 10×10 cm^2 irradiation field inside a tissue-equivalent phantom, at a distance between their centre and the source equal to 100.0 ± 0.2 cm. The samples were irradiated at room temperature under atmospheric pressure with exposures corresponding to 200 MU, 2000 MU and 4000 MU (100 MU correspond to 95.3 cGy).

The wished color change was not observed for the exposed samples. Moreover, the UV-Vis spectra, recorded by Varian Cary 50 Spectrophotometer., did not show the presence of the peak, characteristic of copper nanoparticles formation. Probably, that is due to the fact that a copper salt with a +2 oxidation state was used and, therefore, the reaction $Cu^{2+} + 2e^-_{aq} \rightarrow Cu^0$ is thwarted respect to a reaction where the copper has an oxidation state equal to +1, so as for the Ag salt used in Chapter 2. Moreover, it is necessary to keep present that the collision section of Ag^+ ions is different form that of Cu^+ ions. It has also to be noted that no polymer was used as capping agent for the detector based on silver

nanopaticles precursors. Probably, the PAAm limits the formation of copper nanoparticles, reducing the mobility of Cu^{2+} ions, during the reaction, even if it is useful for the formation of nanoparticles with more uniform dimensions [6]. Indeed, in ref. [7], doses of kGy are necessary to reduce silver nanoparticles in a polyvinilpirrolidone matrix by gamma radiation. These doses are obviously impossible for dosimetrical purposes.

3.2 ZnS nanoparticles precursors

In the past two decades, nanocrystalline ZnS was prepared in the forms of thin film, powder and colloid using different synthesis techniques such as coevaporation [8], wet chemical [9], sol-gel [10], solid state [11], micro-wave irradiation [12], ultrasonic irradiation [13] or synthesis under high-gravity environment [14].

One of the matters faced during the Ph.D. was to understand if ZnS nanoparticles could be synthesized by gamma radiation, so to construct a dosimeter.

To this aim, ZnS nanoparticles precursors were prepared dissolving 1 g of zinc sulphate hydrate ($Zn(NO_3)_2xH_2O$) in 15 ml of ethanol and adding an excess of ammonia, under constant stirring. Then, the resulting solution was mixed with that made by 2 ml of 1-Dodecantiol ($CH_3(CH_2)_{11}SH$) and 10 ml of ethanol. After filtering, washing with ethanol, the sample was dried at room temperature.

Then, films of polystyrene containing ZnS precursors were prepared. This choice is justified by the fact that it is more practical to irradiate a film instead of a liquid. To this end, 1.6 g of polystyrene was dissolved in 40 ml of chloroform and 0.4 g of ZnS precursors were added to the resulting solution.

After drying the films, they were exposed to the 6 MeV photon beam generated by the LINAC (Precise Elekta) of "G. Rummo" Hospital in Benevento. The samples were placed between plastic water sheets on the central part of the 10×10

cm^2 irradiation field at a source-to-sample distance of 100.0 ± 0.2 cm, as in paragraph 2.1.2, and irradiated with doses of 2 Gy and 9 Gy.

The UV-Vis spectra of the irradiated samples were recorded by Varian Cary 50 Spectrophotometer. The absorption spectra of the irradiated sample show an increase respect to not irradiated film, consisting of polystyrene and precursors (Fig. 3.2 a), and respect to not irradiated film consisting only of polystyrene without precursors (Fig. 3.2 b).

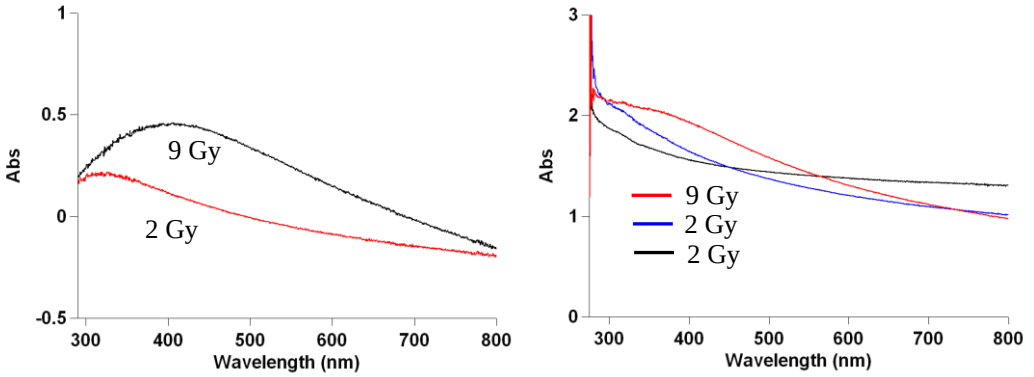

(a) (b)

Fig. 3.2: (a) UV-Vis spectra of the polystyrene films containing ZnS precursors after irradiation with 2 Gy (red line) and 9 Gy (black line). The baseline was the polystyrene film containing ZnS precursors and not irradiated. (b) UV-Vis spectra of the polystyrene films containing ZnS precursors irradiated respectively with 2 Gy (blue line) and 9 Gy (red line) and not irradiated (black line). The baseline was the polystyrene film without precursors and not irradiated.

Since it is not clear if nanoparticles are formed by UV measurements, the diffraction spectra of the irradiated films were recorded by D8 Advance X-ray diffractometer. The absence of the peaks corresponding to the plane of ZnS formation took to the conclusion that the synthesis was not occurred.

Probably, doses of kGy are necessary for the formation of nanoparticles, but these doses are too high for dosimetrical purposes. Another hypothesis is that it was not a good idea to disperse the precursors in a polymer, which could restrict the synthesis reducing ions mobility. These considerations seem to be confirmed by a recent paper [15], published after our experiments, which presents, for the first time, a novel strategy to fabricate chitosan- coated ZnS and ZnS:Mn^{2+} quantum dots in an aqueous system, at room temperature under ambient pressure, via gamma irradiation. The synthesis occurs by doses of kGy and the presence of an aqueous system play an important role. Indeed, when ionizing radiation interacts with water, it produces a range of ions, radicals which enter in the reaction process, allowing nanoparticles synthesis. So, also the medium is crucial for the synthesis.

3.3 Mn doped ZnS nanoparticles

In recent years, also the optical properties of impurity-doped nanocrystals have attracted much attention. In doped compound semiconductors, in contrast with undoped ones, the impurity states play a special role in affecting the electronic energy structures and transition probabilities [16]. For doped nanocrystalline semiconductor compounds, confinement effects in the energy states also produces unusual physical and optical behavior. One of these nanocrystals is Mn^{2+} doped ZnS. Indeed, the doping ions act as recombination centers for the excited electron–hole pairs and this results in strong and characteristic luminescence.

In ref. [17], ZnS:Mn^{2+} nano-crystal phosphor was synthesized for the first time using solid-state method at low temperature from acetate and sodium sulphide. This approach is simple, cheap and convenient method and gives high yields of products. Moreover, by this method, ZnS:Mn^{2+} nanoparticles can be successfully prepared with good reproducibility and high luminescence intensity.

In a typical experiment, 0.1 mol of zinc acetate ($Zn(CH_3COO)_2$), 0.1 mol of sodium sulphide(Na_2S), 0.003 mol of manganese acetate ($Mn(CH_3COO)_2$) were grinding separately for 5 min in agate mortar. Then, they were mixed and ground in the agate mortar for 10 min to get the best possible homogeneity. The crude solid sample, was washed with ethanol, water three times, centrifuged and dried at 110 °C in air for 4 h.

This synthesis was reproduced and the XRD pattern of the products (Fig. 3.3) was recorded by D8 Advance X-ray diffractometer. The sample exhibits zinc blende crystal structure. The three diffraction peaks correspond to the (111), (220) and (311) planes, respectively, of cubic ZnS. No diffraction peaks corresponding to MnS are observed.

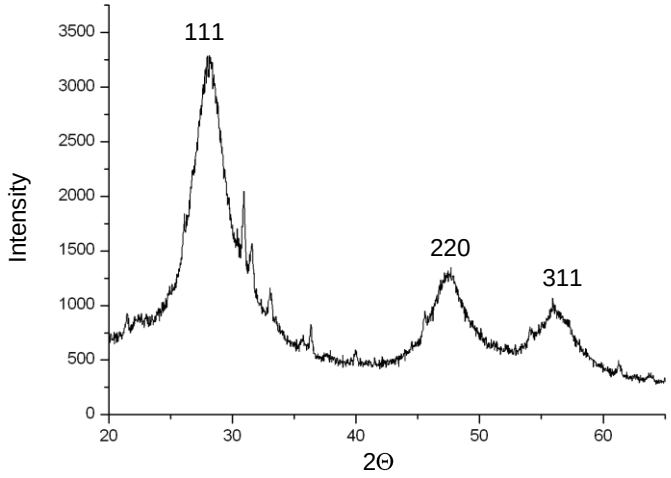

Fig. 3.3: XRD pattern of ZnS:Mn products synthesized from low-temperature solid-state process. 1 cub(111)/hex(002); 2, cub(220)/hex(110); 3, cub(311)/hex(112).

The average crystallite size can be determined from the half-width of the diffraction peaks using Debye–Scherrer equation

$$D = \frac{\alpha\lambda}{\beta\cos\Theta}, \qquad \textit{(Eq. 3.1)}$$

where D is the average crystallite size, α is a geometric factor (equal to 0.89 [17]), λ is the X-ray wavelength (1.54056 Å), and β is the half-width of diffraction peak (measured in radians). Here, the Θ corresponding to the (111) plane was selected. The average crystallite size of the $ZnS:Mn^{2+}$ nanoparticles is about 6 nm, in agreement with ref [17].

Since the synthesized nanoparticles show a strong luminescence [17], our idea was to study the possible changes in the intensity of the photoluminescence spectrum, after radiation.

Having in mind this idea, it was necessary to dissolve the powder in a medium. It was first tried with water without result and then with glycerin. In particular, 0.05 g of $ZnS:Mn^{2+}$ nanoparticles were mixed in 30 ml of glycerin, obtaining a homogeneous suspension. Subsequently, it was necessary to dilute the sample 3 more times, in order to have a transparent solution so to measure the photolumiscence spectrum. The final concentration of the solution was equal to 0.00125 g/ml.

The solution showed an orange-pink color under UV light and it was exposed to the 6 MeV photon beam generated by the LINAC (Precise Elekta) of "G. Rummo" Hospital in Benevento, using the same irradiation set up described in paragraph 2.1.2. The samples were irradiated with doses of 2 Gy, 10 Gy and 20 Gy, respectively.

The photoluminescence spectra of the samples were measured by Cary Eclipse Varian fluorescence spectrophotometer.

In Fig. 3.4 the photoluminescence spectrum of the sample after irradiation of 20 Gy, is shown. A peak of 668 a.u at 530 nm is clear evident.

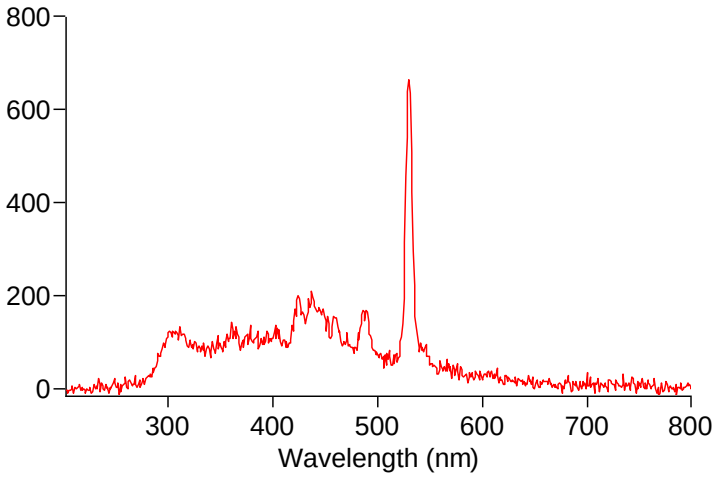

Fig. 3.4: photoluminescence spectrum of the sample after irradiation of 20 Gy.

In Fig. 3.5 the spectra of all the samples, not exposed to radiation and after irradiation, are shown in the range from 500 nm to 600 nm.

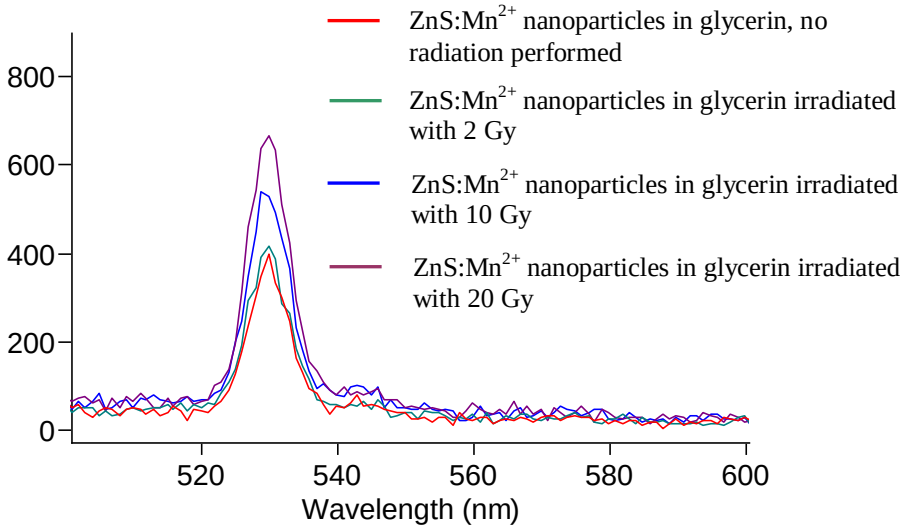

Fig. 3.5: photoluminescence spectra of ZnS:Mn^{2+} nanoparticles in glycerin after irradiation with 20 Gy (violet line), 10 Gy (blue line), 2 Gy (green line). The red line corresponds to the photoluminescence spectrum of the sample not exposed to radiation.

A peak at ~ 530 nm whose intensity grows with dose is evident. The solution irradiated with 2 Gy responds to radiation with a peak intensity of 420.5 a.u., which differs slightly from that of the solution not exposed: the difference is ~ 23 a.u.

The peak intensity shows a linear dependance on the absorbed dose on the explored range (Fig. 3.6).

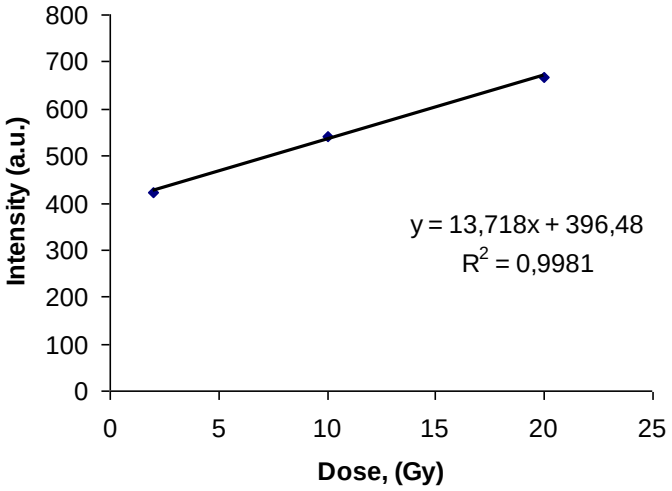

Fig. 3.6: dependence of the photoluminescence peak on the absorbed dose.

So, exposing ZnS:Mn^{2+} nanoparticles to radiation has the effect to increase their photoluminescence and this phenomenon could be used for the construction of a relative dosimeter.

3.4 Bibliography

[1] Gaponenko S.V., Optical Properties Of Semiconductor Nanocrystals, Cambridge University Press,1998.

[2] Trindade, O'Brien P., Pickett N.L., "Nanocrystalline Semiconductors: Synthesis, Properties, and Perspectives". *Chemistry of Materials*, 13(11):3843-3858, 2001.

[3] Murray C.B., Kagan C.R., Bawendi M.G., "Synthesis and characterization of monodisperse nanocrystals and close-packed nanocrystal assemblies". *Annu. Rev. Mater. Sci.*, 30:545-610, 2000.

[4] Shipway A.N., Katz E., Willner I., "Nanoparticle Arrays on Surfaces for Electronic, Optical, and Sensor Applications". *ChemPhysChem*, 1:18-52, 2000.

[5] Blanco-Andujar C., Tung L.D., Thanh N. T. K. "Synthesis of nanoparticles for biomedical applications". *Rep. Prog. Chem.*, Sect. A, 106:553–568, 2010. |

[6] Wang Y., Asefa T., "Poly(allylamine)-Stabilized Colloidal Copper Nanoparticles Synthesis, Morphology, and Their Surface-Enhanced Raman Scattering Properties". *Langmuir*, 26(10), 2010, pp. 7469-7474.

[7] Gasaymeh S.S., Radiman S., Heng L.Y., Saion E., Saeed G.H.M. "Synthesis and Characterization of Silver/Polyvinilpirrolidone (Ag/PVP) Nanoparticles Using Gamma Irradiation Techniques". *American Journal of Applied Sciences*, 7(7):892 – 901, 2010.

[8] R. Thielsch R., Böhme T., Böttcher H., "Optical and Structural Properties of Nanocrystalline ZnS-SiO2 Composite Films". *Physica Status Solidi A*, 155:157-170, 1996.

[9] Wei Chen W., Wang Z., Lin Z., Lin L., "Absorption and luminescence of the surface states in ZnS nanoparticles". *Journal of. Applied Physics*, 82, 3111-3115, 1997.

[10] Bhattacharjee B., Ganguli D., Chaudhuri S., Pal A.K., "Synthesis and optical characterization of sol–gel derived zinc sulphide nanoparticles confined in amorphous silica thin films". *Materials Chemistry and Physics*, 78(2); 372-379, 2003.

[11] Lu H.Y., Chu S.-Y., Tan S.-S., "The characteristics of low-temperature-synthesized ZnS and ZnO nanoparticles". *Journal of Crystal Growth*, 269(2-4):385-391, 2004.

[12] Zhao Y., Hong J.-M. and Zhu J.-J., "Microwave-assisted self-assembled ZnS nanoballs". *Journal of Crystal Growth*, 270(3-4):438-445, 2004.

[13] J.F. Xu, W. Ji, J.Y. Lin, S.H. Tang and Y.W. Du, "Preparation of ZnS nanoparticles by ultrasonic radiation method". *Applied Physics A*, 66(6):639-641, 1998.

[14] Chen J., Lia Y., Wanga Y., Yunb J. and Dapeng Caob, "Preparation and characterization of zinc sulfide nanoparticles under high-gravity environment". *Materials Research Bulletin*, 39(2):85-194, 2004.

[15] Chang S., Kang B., Dai Y., Zhang H. and Chen D., "One-step fabrication of biocompatible chitosancoated ZnS and ZnS:Mn^{2+} quantum dots via a γ-radiation Route". *Nanoscale Research Letters*, 6:591-597, 2011.

[16] Soo Y.L, Ming Z.H., Huang S.W., Kao Y.H., "Local structures around Mn luminescent centers in Mn-doped nanocrystals of ZnS". *Physical Review B*, 50:7602–7607, 1994.

[17] Xi-Bin Yu, Li-Hong Mao, Zhang-Fan, Liang-Zhun Yang, Shi-Ping Yang, "The synthesis of ZnS:Mn^{2+} nano-particles by solid-state method at low temperature and their photoluminescence characteristics". *Materials Letters*, 58: 3661–3664, 2004.

CHAPTER 4

MWCNTs AND GRAPHENE BASED DOSIMETERS

Ionization chambers are considered the most important dosimeters because they allow absolute dose measurements and are characterized by high accuracy, stability over time and reliability. However, they have a relative large physical size which limits their spatial resolution and require a high bias voltage to achieve an acceptable collection of charges, excluding their use for in vivo dosimetry. These disadvantages require the implementation of ionization chambers with improved electrodes. In this context, parallel plate ionization chambers with electrodes based on a forest of vertically aligned Multiwall Carbon Nanotubes (MWCNTs) and graphene were designed and fabricated [1, 2]; their charge collection efficiency was studied and their performance was compared with that of electrodes made of a conventional material. Moreover, in order to highlight the effect of nanocarbons, reference radiation detectors were also tested.

Nanocarbons for their low production cost and the fascinating physical properties [3], are very promising materials to obtain a new generation dosimeter, allowing a net scale passage.

The MWCNTs containing electrode consists of a silicon wafer as patterned substrate for the deposition of catalytic nanoparticles (NPs). The NPs are active for MWCNT controlled growth to form a very regular nanotubes forest (several

tubes of controlled geometry in terms of length, diameter and wall thickness). A specific advantage comes from the possibility to grow nanotubes directly on silicon, the most consolidated support for nanodevice development, integrating the electrode production in the silicon technology, e. g. CMOS technology. A less expensive micro-contact printing than the electron beam lithography (EBL) was used for the nanoparticles patterning.

For the graphene containing electrodes, the growth was done by catalytic chemical vapor deposition on a copper substrate.

The proposed ionization chambers with electrodes based on nanocarbons display an excellent linear response to dose and collect more charge than tested ones devices (both made of conventional material and reference materials) at a standard bias voltage. This allows constructing miniaturized ionization chambers, improving spatial resolution. The detector with the best charge collection efficiency was that realized with aluminum cathode and silicon-MWCNTs anode. Moreover, this was the only detector able to collect charge also to zero volt, opening perspectives for in vivo applications. Measurements of the collected charge vs. bias voltage and electrodes distance were also performed for this dosimeter. It was found an exponential dependence on bias voltage and the possibility to collect more charges reducing the distance between the electrodes. As regards the performance of graphene electrodes, they were able to collect more charge than reference ones at a standard bias voltage but, at its decreasing, the charge collection efficiency becomes worst, likely due to a graphene semiconductor behavior.

In this chapter, the ionization chambers design, the synthesis of nanomaterials, their characterization and their response to radiation are presented.

4.1 Synthesis of MWCNT and graphene

For the patterned growth of multiwall carbon nanotubes forest catalytic chemical vapor deposition (CCVD) using monodispersed nickel ferrite nanoparticles ($NiFe_2O_4$) as catalyst was performed. Graphene was prepared by CCVD on a Cu foil.

4.1.1 Preparation of the patterned catalyst for the MWCNTs synthesis

For the preparation of $NiFe_2O_4$ nanoparticles, phenyl ether (99%, 10mL), 1,2-hexadecanediol (97%, 10mmol), oleic acid (90%, 6mmol), oleylamine (>70%, 6mmol), Ni(II)acetylacetonate ($Ni(acac)_2$, 1mmol), Iron(III) acetylacetonate ($Fe(acac)_3$, 1mmol) were purchased from Aldrich Chemical Co, mixed and magnetically stirred under nitrogen flow. The mixture was heated to 265°C for 30 min. Then, the black-brown mixture was cooled to room temperature, ethanol was added and the black material was precipitated and separated via centrifugation. The products were dispersed in hexane and stored in a vial.

The $NiFe_2O_4$ nanoparticles were patterned on silicon wafer SiO_2/Si by microcontact printing using a Polysimethylsiloxane (PDMS) stamp. A schematic representation of the micro-contact printing procedure is shown in Fig. 4.1: a nanoparticles dispersion was deposited on a PDMS stamp, after evaporation a self assembly monolayer covers the PDMS surface, and finally by nanoparticles printing a patterned substrate was obtained.

PDMS stamps for transfer printing were made by using SYLGARD 184 silicone elastomer kit with a silicon substrate as master.

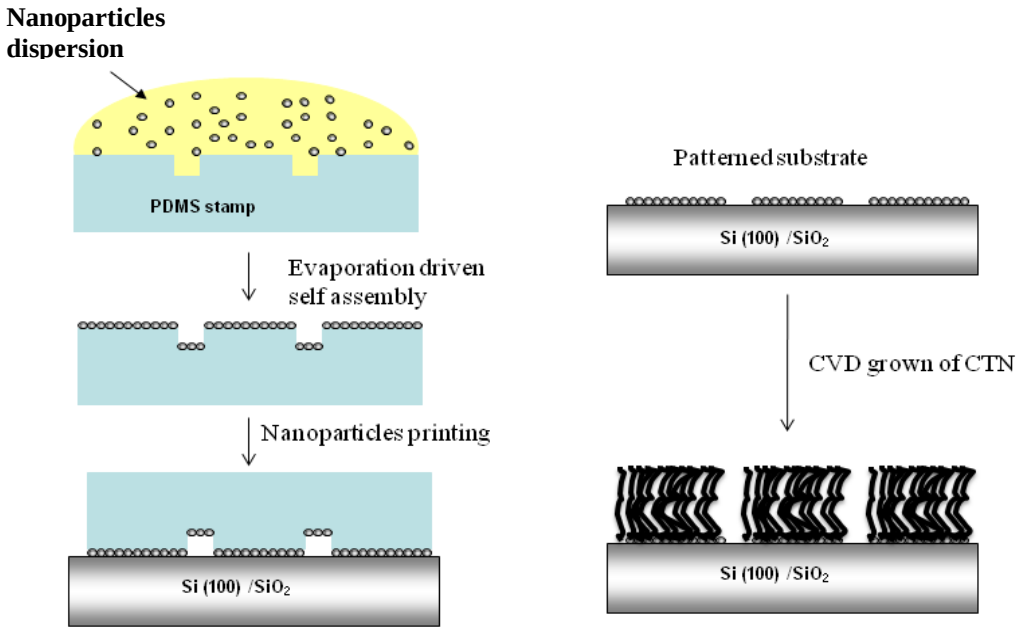

Fig. 4.1: schematic representation of the micro-contact printing procedure.

4.1.2 CCVD growth of Multiwall Carbon Nanotubes

To synthesize MWCNTs, the silicon substrate was placed into a vertical quartz tube reactor and maintained at room temperature in 80(stp)cm^3/min N_2 flow for 4 min. The reactor was then introduced in a pre-heated furnace at 800°C for 10 min. After replacing the pure N_2 flow by a gas mixture of C_2H_4 (99.998% purity, 8 (stp)cm^3/min flow rate) and N_2 (99.999% purity, 72 (stp)cm^3/min flow rate), the reactor was maintained at 800°C for 10min. After the reaction the quartz tube was cooled down to room temperature under N_2 flow.

4.1.3 CCVD growth of graphene

Graphene layers were grown by CCVD of methane diluted in nitrogen; mass flow controllers (M.F.C.) assured constant flow rate for each gas. The synthesis was performed in isothermal conditions at 950°C, 100 (stp)cm^3/min flow rate, after 40

min heating treatment of the foil from room temperature up to the synthesis temperature. The average cooling rate after the synthesis was 2°C/min.

4.2 $NiFe_2O_4$ nanoparticles, MWCNTs and graphene characterization

The morphological and structural properties of the nickel ferrite nanoparticles were investigated by transmission electron microscopy (TEM) analysis. TEM micrographs were obtained using a FEI Tecnai electron microscope operating at 200 kV. In Fig. 4.2 are reported the TEM images of nickel ferrite nanoparticles at two different magnifications. The images reveal the formation of highly uniform particles that, once deposited over a carbon coated copper grid, tend to self-organize in regular hexagonal lattices.

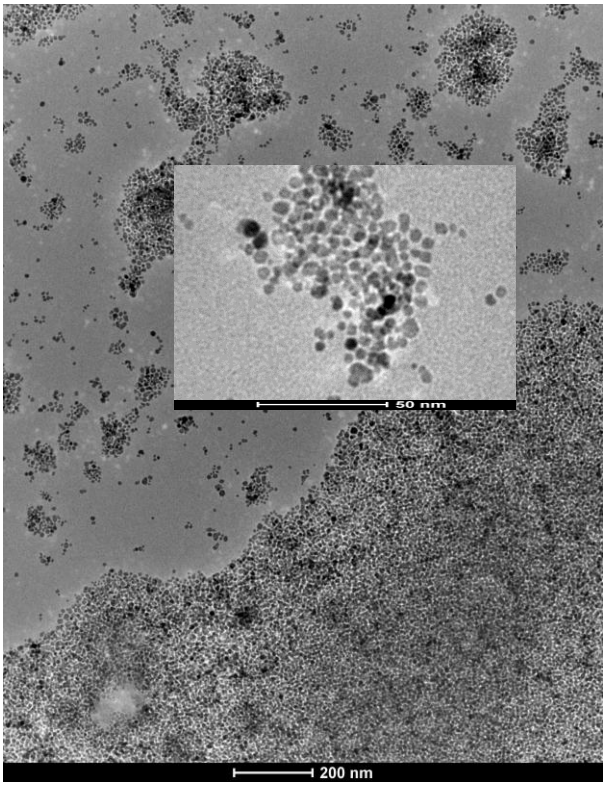

Fig. 4.2: TEM image of nanoparticles prepared by a “wet chemistry” approach.

The size distributions obtained from a statistic analysis over 100 nanoparticles indicate that they have a size of 4.6 nm with a standard deviation of 0.8 nm. The temperature of nanoparticles synthesis is a critical parameter for the formation of nanocrystals and for their growth [4].

In Fig. 4.3, a cross section of a silicon wafer after CCVD synthesis is shown. The formation of vertically aligned CNT forest on the substrate is clearly observed. The thickness of CNT film is ≈12 μm. The images in Fig. 4.3 were collected with a SEM LEO 125 VP microscope.

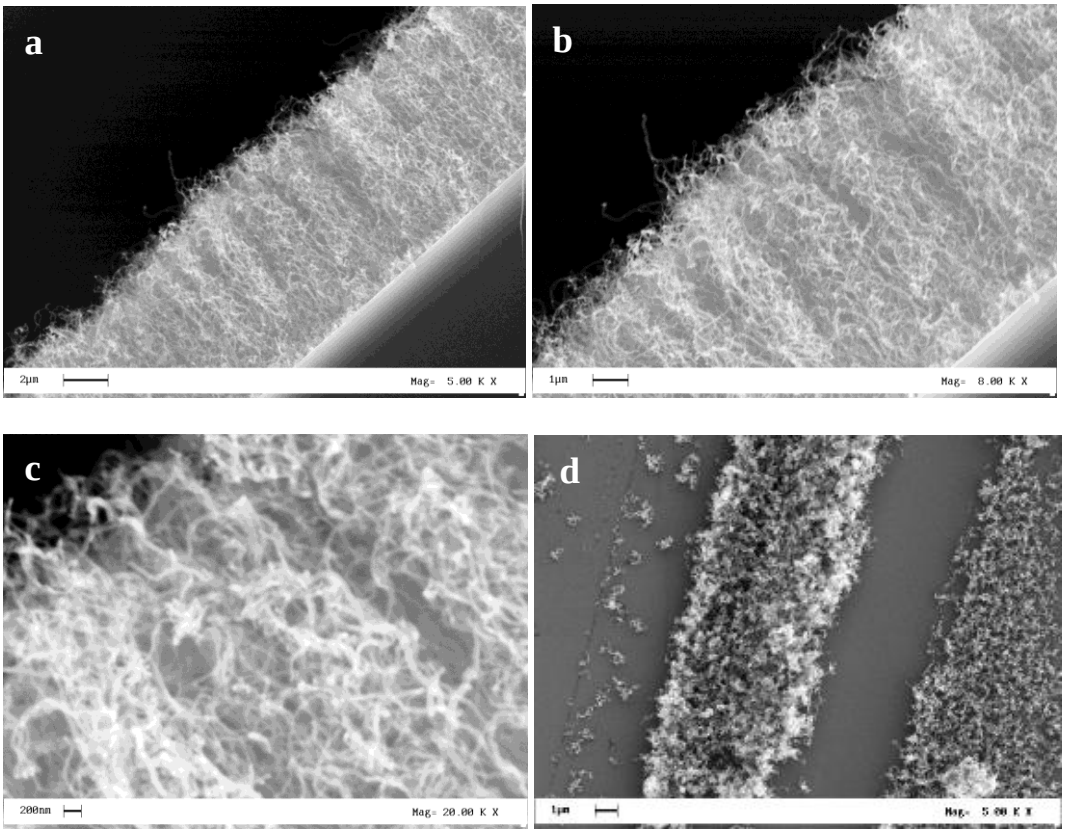

Fig. 4.3: SEM images of carbon nanotubes grown by CCVD on silicon substrate. (a, b, c) Film edge at different magnification; (d) patterned substrate.

As regards graphene characterization, the presence of few layers graphene on the surface of copper is revealed by the Raman spectra (Fig. 4.4), obtained with a micro Raman spectrometer Renishaw inVia (514 nm excitation wavelength).
In particular, the so-called G band appearing at 1582 cm^{-1} and the G' or 2D band at about 2700 cm^{-1} [5-6] are present. The G' band at room temperature can be easily fitted with 6 Lorentzian features as typical of 3 layers graphene [5]. A D-band, due to disorder or edge [7] of a graphene sample, can be also seen at about half of the frequency of the G' band (around 1350 cm^{-1} using laser excitation at 2.41 eV).

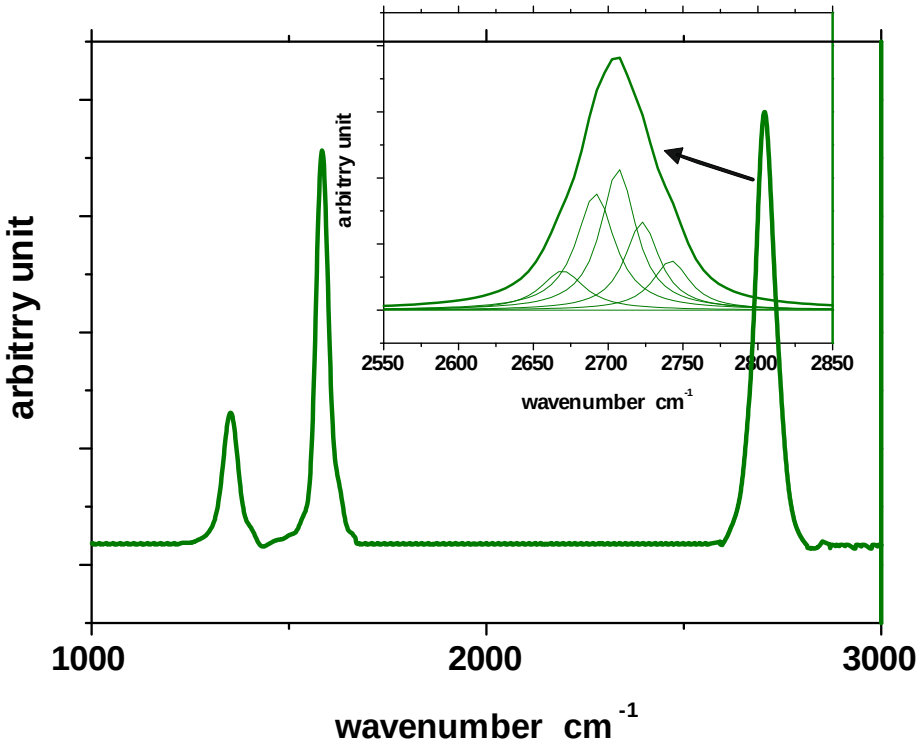

Fig. 4.4. Raman spectrum of graphene on Cu foil.

XRD measurements were also performed with a Bruker D8 X-ray diffractometer using CuKα radiation. In Fig. 4.5, the X-ray diffraction patterns of copper, before

and after graphene coating, are reported. In the pattern of the original copper the typical (111), (100) and (110) peaks of polycrystalline Cu are visible [8], the spectrum also clearly evidences the no so high level of the original order. The Cu foil appears practically monocristalline after the synthesis. It is worth to notice the absence of the (002) diffraction peak at about 26° (2Θ), typical of graphite stacking, even if carbon is present.

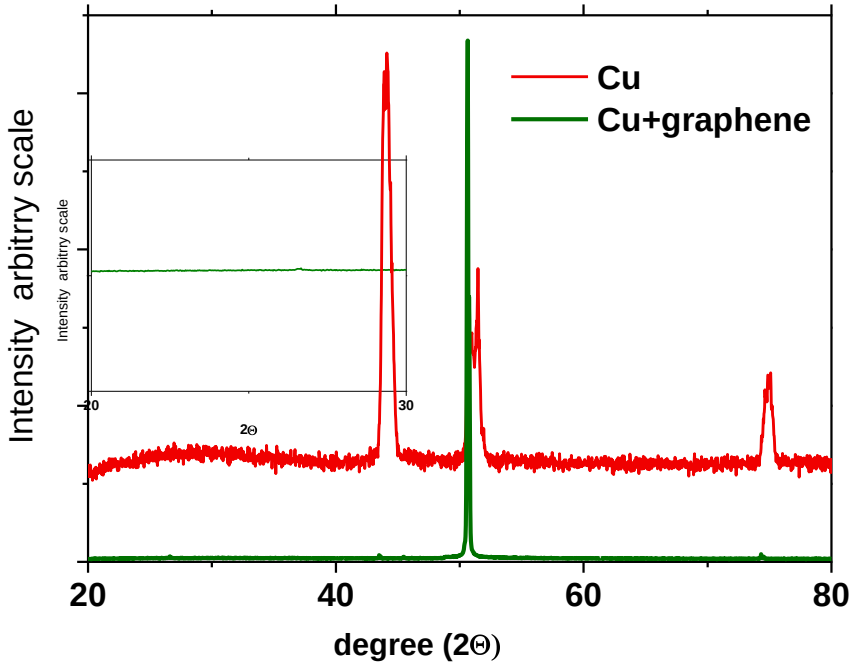

Fig. 4.5: X-ray diffraction pattern of Cu and Graphene on Cu.

4.3 Sensor device

The working principle of a ionization chamber is illustrated in paragraph 1.4.

Parallel plate ionization chambers with electrodes of different materials were prepared and their response to radiation was studied, in order to perform a

comparison between their performances. In particular, electrodes with copper, aluminum, silicon, silicon covered with a forest of vertically aligned MWCNTs and copper covered with graphene were realized. With these electrodes, seven ionization chambers were assembled according to Table 4.1. Specifically, electrodes containing nanocarbons were compared with reference electrodes without carbon nanotubes and graphene. The copper anode was treated in the same operating condition as for the graphene synthesis but in the absence of methane. Also an ionization chamber containing electrodes made of conventional material (such as aluminum) has been tested for comparison.

Cathode	**Anode**
Aluminum	Silicon
Aluminum	MWCNTs forest on silicon
Aluminum	Aluminum
Aluminum	Graphene covered copper
Aluminum	Copper
Graphene covered copper	Graphene covered copper
Copper	Copper

Tab. 4.1: materials for ionization chambers electrodes.

The two electrodes of each ionization chamber were held by the basis of a cylindrical plastic container at a distance from each other of 12 mm. The gas inside the chamber was air. In Fig. 4.6, different views of our ionization chamber prototype are represented, while, in Fig. 4.7, a representation of MWCNTs/silicon electrode (a) and graphene/Cu electrode (b) is shown.

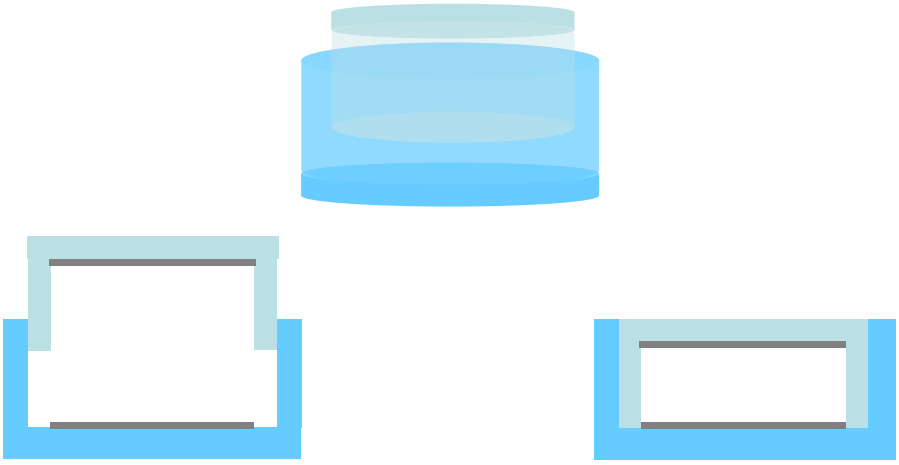

Fig. 4.6: schematic views of ionization chamber prototype.

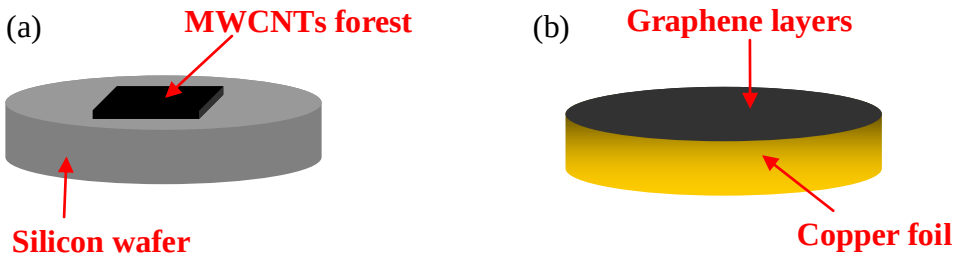

Fig. 4.7: (a) silicon-MWCNTs electrode and (b) copper-graphene electrode.

A bias voltage respectively of 310 V, 155 V and 0 V was applied and the collected charge was measured by reference level electrometer (SUN Nuclear Corporation), connected to the electrodes via a low noise cable. For conventional parallel plate ionization chambers, usually, the best efficiency of charge collection occurs at high voltages between 200 and 400V.

4.4 Experimental irradiation set up

All the sensors were exposed to the 6 MeV photon beam generated by the LINAC (ELEKTA Synergy) of Check up Diagnostic Center. The experimental irradiation

set up was equal to that used for radiochromic film of paragraph 1.5.3 and for Ag nanoparticle precursors based detector of Chapter 2: the sensors were placed at the centre of a 10×10 cm^2 irradiation field inside a tissue-equivalent phantom, at a distance between their centre and the source equal to 100.0 ± 0.2 cm. The sensors were irradiated at room temperature under atmospheric pressure with exposures corresponding to 21 MU, 50 MU and 105 MU. In this reference set-up, 100 MU correspond to 95.3 cGy.

4.5 Irradiation measurements results

Firstly, irradiation measurements with all seven detectors were carried out at 21 MU, 50 MU and 105 MU and at fixed bias voltage of 310 V. The collected charge shows an excellent linear dependence on dose for all the ionization chambers (Fig. 4.5 a-b), a necessary characteristic for an efficient dosimeter. Moreover, our nanomaterial based radiation sensors collect more charge than the other tested electrodes (Figure 4.8 a-b). This is an interesting result for the fabrication of a miniaturized ionization chamber.

The comparison of detector performances indicates that the best charge collection efficiency was obtained with the device having the aluminum cathode and the silicon-MWCNTs anode (Fig. 4.8 a-b). The slope of the straight line is more than the double with respect to that of ionization chamber realized with aluminum cathode and silicon without MWCNTs anode (Fig. 4.8 a). Therefore, the addition of the forest of nanotubes on the silicon has a great benefit on the charge collection efficiency. This result is apparently in contrast with findings of ref. [9], where electrodes of stainless steel with randomly CNT nanotubes were constructed and compared with electrodes of stainless steel alone that exhibited a lower performance. In that reference it was suggested that the use of purified CNTs could give a better result.

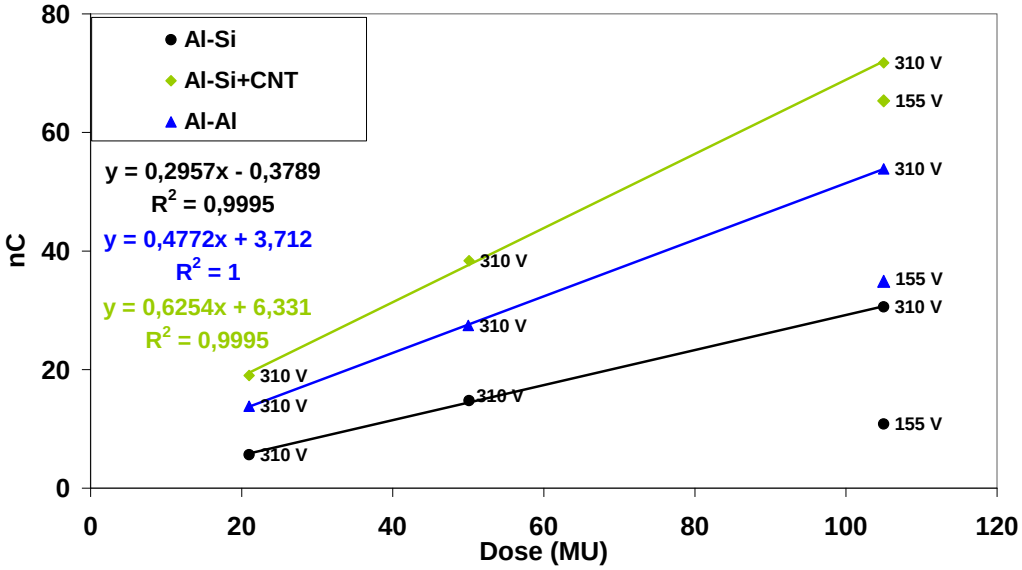

(a)

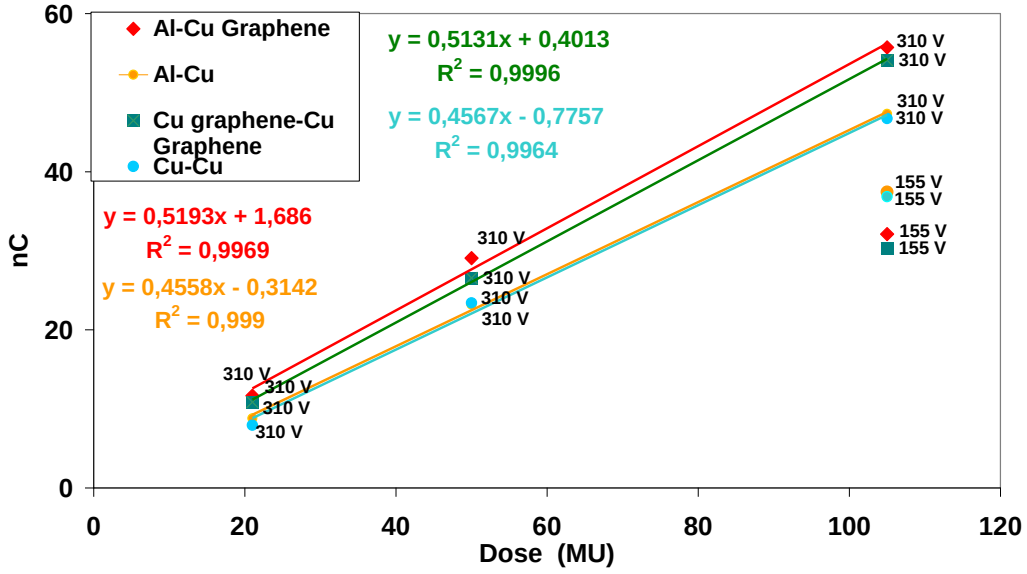

(b)

Fig. 4.8: collected charge at 310 V vs. dose for all ionization chambers. Comparison between the collected charge at 105 MU and 310 V and that at 105 MU and 155V.

Moreover, it is our opinion that the use of vertically aligned MWCNTs, that exhibit billion of sharp tips, instead of randomly CNT nanotubes as in [9], improves the collection efficiency of radiation detector. So, the geometry plays an important role. This statement is confirmed by the results of our second set-up of measurements performed at lower bias voltage (155 V) and at an exposure of 105 MU. Comparing the collected charge at 310 V with that at 155 V, it is clear that the difference between these two values is smaller when aluminum cathode and silicon-MWCNTs anode are used (Fig. 4.8 a-b).

Furthermore, it is was found that MWCNTs ionization chamber is able to collect charge also at 0 V. This is clear in Fig. 4.9, where the collected charge is plotted vs. the bias voltages, at exposure of 105 MU. The collected charge shows an exponential dependence on bias voltage and it is different from zero at no bias voltage. By increasing the bias voltage, the electric field between the electrodes becomes stronger and the detector is able to collect more charge, until a plateau is reached. It has to be noticed that only MWCNTs based detector is able to collect charge at 0 V. This behavior was not found for the other tested ionization chambers.

The response of MWCNTs ionization chamber was also studied at different doses maintaining the bias voltage at 0 V and reducing the electrodes distance from 12 mm to 6 mm. Also in this case, the collected charge shows a linear response by dose (Fig. 4.10). Moreover, the value of the collected charge at 105 MU is almost the double of that obtained at the same exposure but at an electrodes distance of 12 mm (Fig. 4.10). Halving the electrodes distance has the effect to double the collected charge in agreement with the law of condenser capacity.

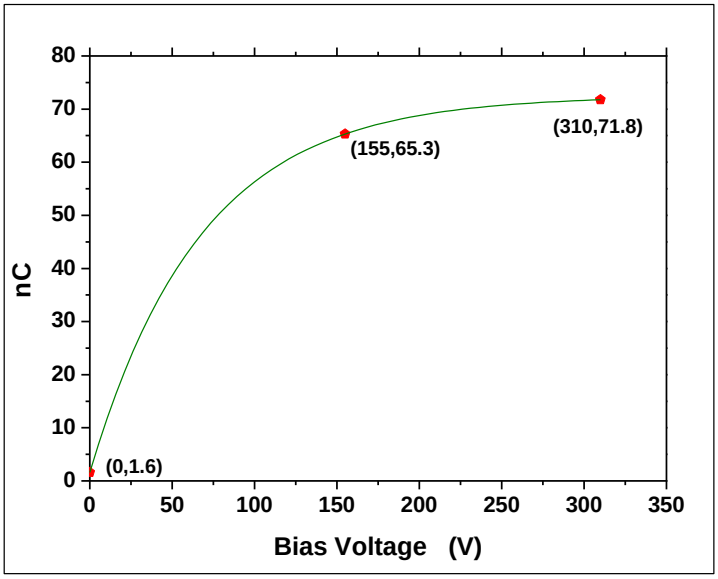

Fig. 4.9: collected charges vs. bias voltage for ionization chamber with silicon-MWCNTs anode and aluminum cathode at a distance of 12 mm.

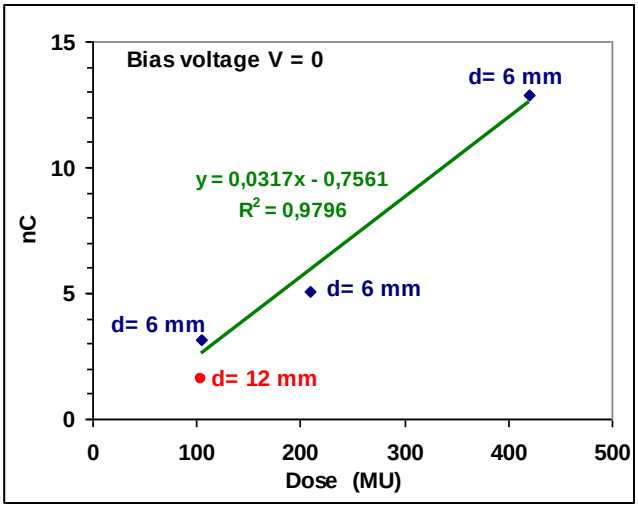

Fig. 4.10: collected charges at 0 V vs. dose for ionization chamber with silicon-MWCNTs anode and aluminum cathode at a distance of 6 mm (blue indicators). Collected charge at 0 V and 105 MU (red indicator) for the same device with a distance between the electrodes equal to 12 mm.

Graphene ionization chambers (both copper/graphene anode-aluminum cathode and copper/graphene anode-copper/graphene cathode) at 310 V bias voltage achieve a better charge collection than the reference ionization chambers (Fig. 4.8 b). At 155 V the results are upset: the electrodes of graphene collect minor charge than their corresponding reference electrodes with no graphene. So graphene grown on copper seems to show a semiconductor behavior. In ref. [10], it was reported that the electronic gap of graphene can be controlled externally by applying a gate bias. Moreover, the electronic properties of graphene can be strongly influenced by interactions with the substrate [11].

4.6 Bibliography

[1] Funaro M., Sarno M., Altavilla C., Proto A., Ciambelli P. "Dosimetro di radiazione "in tempo reale" basato su nanomateriali di carbonio". Patent SA 2012°000011.

[2] Funaro M., Sarno M., Ciambelli P., Altavilla C., Proto A. "Real time radiation dosimeters based on vertically aligned Multiwall Carbon Nantotubes and Graphene". Submitted, 2012.

[3] Wong H.S.P., Akinwande D. "Carbon Nanotube and Graphene Device Physics". Cambridge University Press, 2010.

[4] Altavilla C., Sarno M., Ciambelli P. "Synthesis of Ordered Layers of Monodisperse $CoFe_2O_4$ Nanoparticles for Catalyzed Growth of Carbon Nanotubes on Silicon Substrate". *Chemistry of Materials*, 21:4851–4858, 2009.

[5] Malard L.M., Pimenta M.A., Dresselhaus G., Dresselhaus M.S., "Raman spectroscopy in graphene". *Physic Reports*, 473(5-6):51–87, 2009.

[6] Ferrari A.C. "Raman spectroscopy of graphene and graphite: Disorder, electron-phonon coupling, doping and nonadiabatic effects". *Solid State Communication*, 143:47–57, 2007.

[7] Pimenta M.A., Dresselhaus G., Dresselhaus M.S., Cançado L.G., Jorio A., Saito R. "Studying disorder in graphite-based systems by Raman spectroscopy". *Physical Chemistry Chemical Physics*, 9:1276–1291, 2007.

[8] Rasool H.I., Song E.B., Allen M.J., Wassei J.K., Kaner R.B., Wang K.L., Weiller B.H., Gimzewski J.K. "Continuity of Graphene on Polycrystalline Copper". *Nano Letters*, 11:251–256, 2011.

[9] Ma J., Yeow J.T.W., Chow J.C.L and Barnett R.B. "A carbon nanotube-based radiation sensor". *International Journal of Robotics and Automation*, 22(1):49–58, 2007.

[10] Castro E.V., Novoselov K.S., Morozov S.V., Peres N.M.R., Lopes dos Santos J.M.B., Nilsson J., Guinea F., Geim A.K., and Castro Neto A.H. "Biased Bilayer Graphene: Semiconductor with a Gap Tunable by the Electric Field Effect". *Physical Review Letter*, 99(216802):1–4, 2007.

[11] Gao L., Guest J.R., Guisinger N.P. Epitaxial Graphene on Cu(111). *Nano Letters*, 10:3512–3516, 2010.

CHAPTER 5
SILVER NANOPARTICLES IN ALANINE

As further research activity, silver nanoparticles were synthesized by a green method at room temperature, reducing silver nitrate in aqueous solution by ascorbic acid as reducing agent with the assistance of alanine as capping agent.
The silver nanoparticles were characterized by X-Ray Diffraction (XRD), Scanning Electron Microscopy (SEM) and Transmission Electron Microscopy (TEM). The results of these characterizations show that the use of alanine in the synthesis influences the shape and the dimensions of nanoparticles.
The idea to synthesize silver nanoparticles in alanine stems from the consideration that alanine dosimeters [1] have been introduced on the market and the successful application of silver nanoparticles precursors as radiation detector (Chapter 2) [2].
As illustrated in paragraph 1.9, one of the disadvantages of alanine dosimeters is their high detection threshold (10 Gy), which excludes their use for conventional radiotherapy. For this reason, it is necessary to low their detection threshold, i.e. to improve their sensibility. This could occur with silver/alanine nanocomposites based dosimeters.
In this chapter, the synthesis of silver nanoparticles in alanine and their characterization are presented.

5.1 Synthesis of silver nanoparticles

Silver nanoparticles were prepared by a novel and simple green method at room temperature, reducing silver nitrate in aqueous solution by ascorbic acid as reducing agent with the assistance of alanine as capping agent. To this end, 0.01 mol of silver nitrate ($AgNO_3$, ACS-ISO, Carlo Erba) were first dissolved in 50 ml of distilled water and, then, L-alanine ($C_3H_7NO_2$, 98%, Sigma-Aldrich) was added to this solution. In particular, two solutions with a different ratio between silver and alanine moles were prepared by varying the amount of L-alanine. The $n_{AgNO_3} / n_{C_3H_7NO_2}$ ratios were equal to 0.36 and 0.18. Subsequently, 25 ml of a 0.5 M acid ascorbic solution ($C_6H_8O_6$, 99%, Sigma- Aldrich) were slowly dripped to the above solutions, under constant stirring. The ratio between n_{AgNO_3} and $n_{C_6H_8O_6}$ was almost equal to 1. After acid ascorbic was added, precipitate was formed.

In order to analyze the effects of alanine on silver nanoparticles formation, the same silver nitrate solution without alanine was also prepared and ascorbic acid was added to it.

5.2 XRD characterization

For XRD analysis, the precipitates were collected by filtration, washed and dried. The diffraction patterns were recorded with a D8 Advance X-ray diffractometer (Cu-Kα X-rays of wavelength λ = 1.54056 Å), in the 2Θ range from 10° to 90°.

The typical powder XRD pattern of the sample without alanine is shown in Fig. 5.1. The data shows diffraction peaks at 2Θ = 38.1°, 44.3°, 64.5°, 77.4°, and 81.6°, which can be indexed to (111), (200), (220), (311), and (222) planes of pure silver with face centred cubic symmetry (Joint Committee on Powder Diffraction Standards (JCPDS), silver file No. 04–0783). The high intense peak for FCC

materials is generally (111) reflection, which is observed in the sample. The average crystallite size was estimated by Debye-Scherrer formula (Eq. 3.1). In particular, five values of the average crystallite size, one for each diffraction peak, were computed (Tab. 5.1).

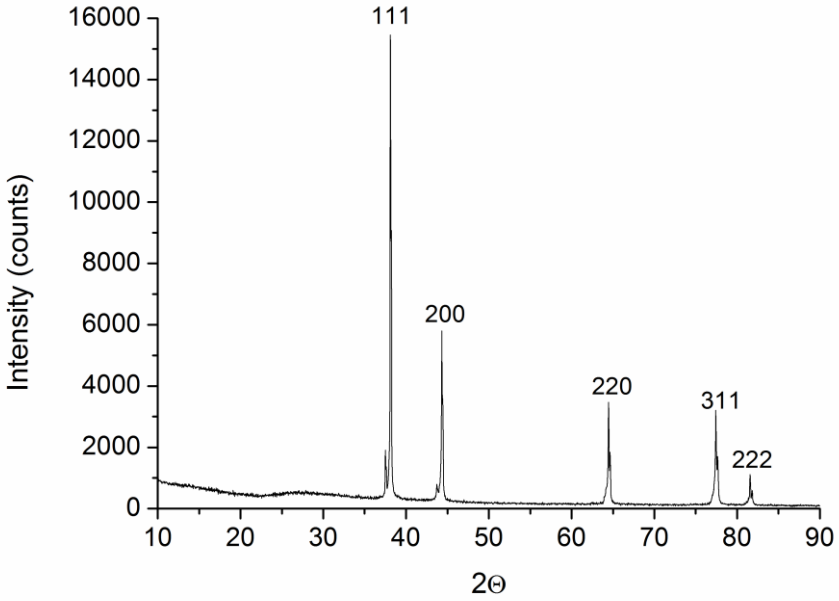

Fig. 5.1: XRD pattern of the sample without alanine.

hkl	2Θ	Half-width of the peak (β)	Average crystallite size (nm)
111	38.1°	0.156	53.3
200	44.3°	0.194	43.7
220	64.5°	0.193	48.1
311	77.4°	0.247	40.8
222	81.6°	0.145	71.6

Tab. 5.1: average crystallite size computed for each diffraction peak for the sample with no alanine.

The typical powder XRD pattern of the sample with a quantity of alanine, so that $n_{AgNO_3} / n_{C_3H_7NO_2} = 0.36$, is shown in Fig. 5.2. The average crystallite size was computed (Tab. 5.2) for each diffraction peak (2θ = 38.2°, 44.3°, 64.5°, 77.4°, and 81.6°), using Debye-Scherrer formula.

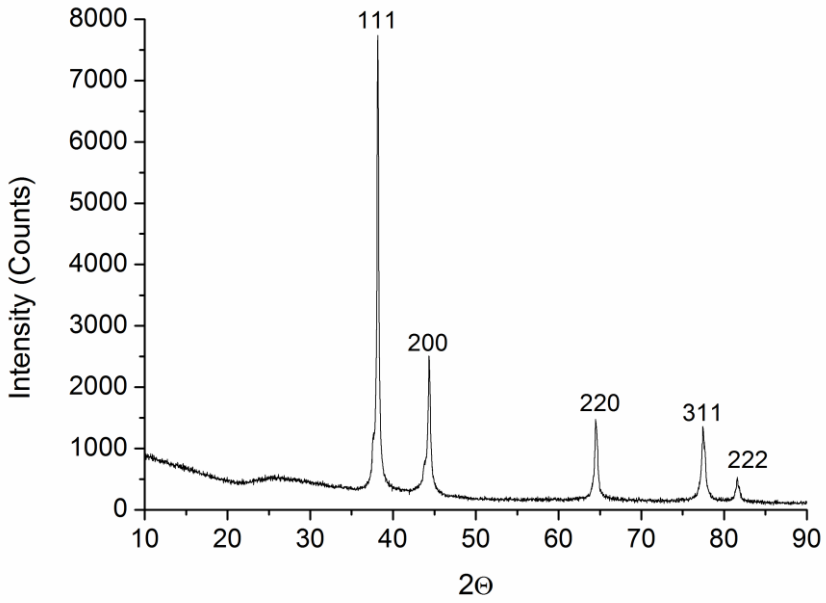

Fig. 5.2: XRD pattern of the sample with alanine ($n_{AgNO_3} / n_{C_3H_7NO_2} = 0.36$).

hkl	2Θ	Half-width of the peak (β)	Average crystallite size (nm)
111	38.2°	0.242	34.4
200	44.3°	0.327	26.0
220	64.5°	0.413	22.5
311	77.4°	0.480	21.0
222	81.6°	0.500	20.8

Tab. 5.2: average crystallite size, computed for each diffraction peak, for the sample with alanine ($n_{AgNO_3} / n_{C_3H_7NO_2} = 0.36$).

The typical powder XRD pattern of the sample with a double quantity of alanine, ($n_{AgNO_3} / n_{C_3H_7NO_2} = 0.18$), is shown in Fig. 5.3.

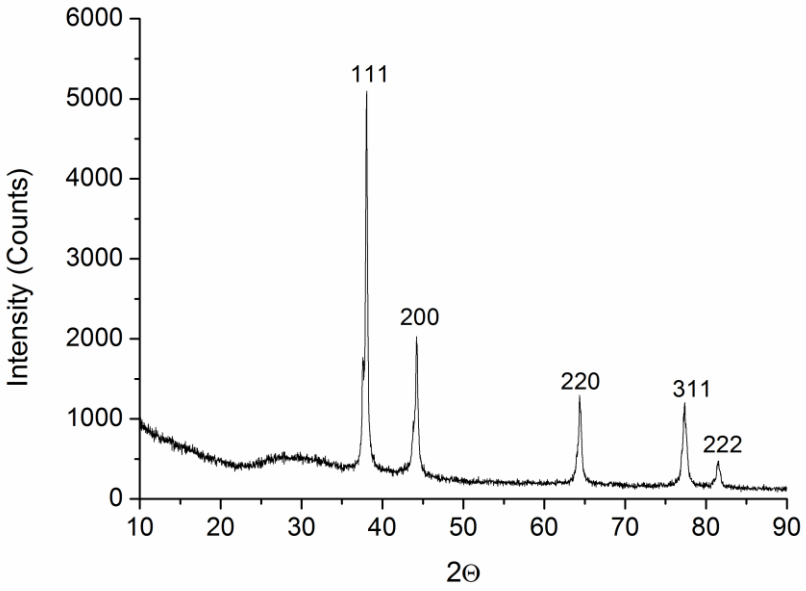

Fig. 5.3: XRD pattern of the sample with alanine ($n_{AgNO_3} / n_{C_3H_7NO_2} = 0.18$).

The average crystallite size was computed (Tab. 5.3) for each diffraction peak (2θ = 38.1°, 44.2°, 64.4°, 77.4°, and 81.6°), using Debye-Scherrer formula.

hkl	2Θ	Half-width of the peak (β)	Average crystallite size (nm)
111	38.1°	0.267	31.1
200	44.2°	0.330	25.6
220	64.4°	0.397	23.4
311	77.4°	0.553	18.2
222	81.6°	0.550	18.9

Tab. 5.3: average crystallite size, computed for each diffraction peak, for the sample with alanine ($n_{AgNO_3} / n_{C_3H_7NO_2} = 0.18$).

Comparing the values of Tab. 5.1, Tab. 5.2, Tab. 5.3, it is evident that the average crystallite size is smaller when alanine is used and that there is not a significant difference between the two samples with alanine.

5.2 SEM characterization

The morphology analysis was performed with a SEM LEO 125 VP microscope. For SEM analysis, the solutions with the precipitates were extolled and washed with distilled water, for three times. Then, a drop of the solution, containing the sample, was applied to the grid. After drop evaporation, the analysis was performed. The images of Fig. 5.4 put in evidence that alanine influences the dimensions and the shape of particles. From Fig. 5.5, it seems that there is not a significant difference between the samples with a different quantity of alanine, in agreement with XRD analysis. The dimensions of the particles with no alanine seem bigger than those obtained by XRD analysis. This is probably due to the presence of non crystalline zone and to surface/volume effects.

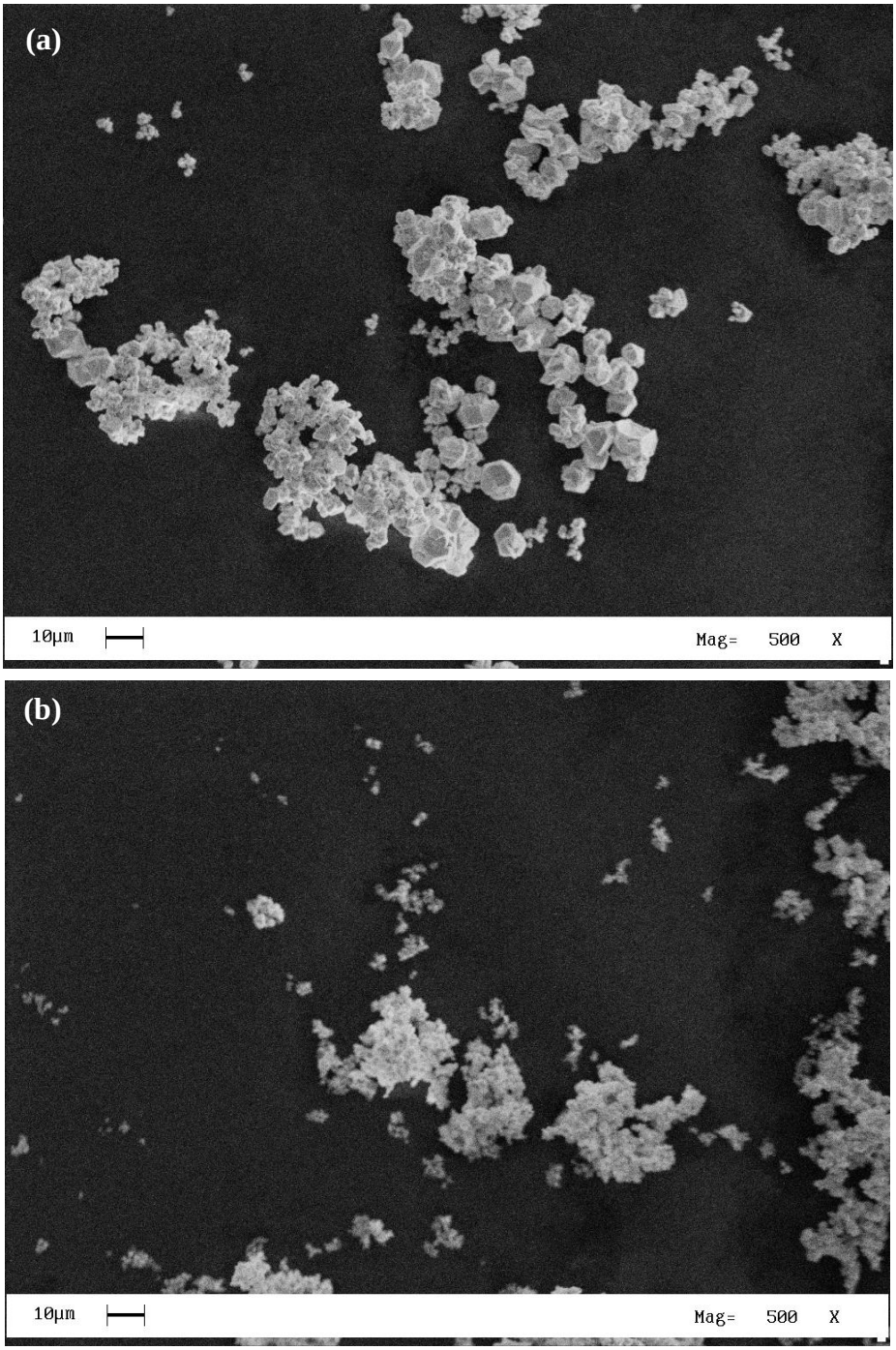

Fig. 5.4: SEM images for the sample without alanine (a) and with a quantity of alanine so that $n_{AgNO_3} / n_{C_3H_7NO_2} = 0.36$ (b).

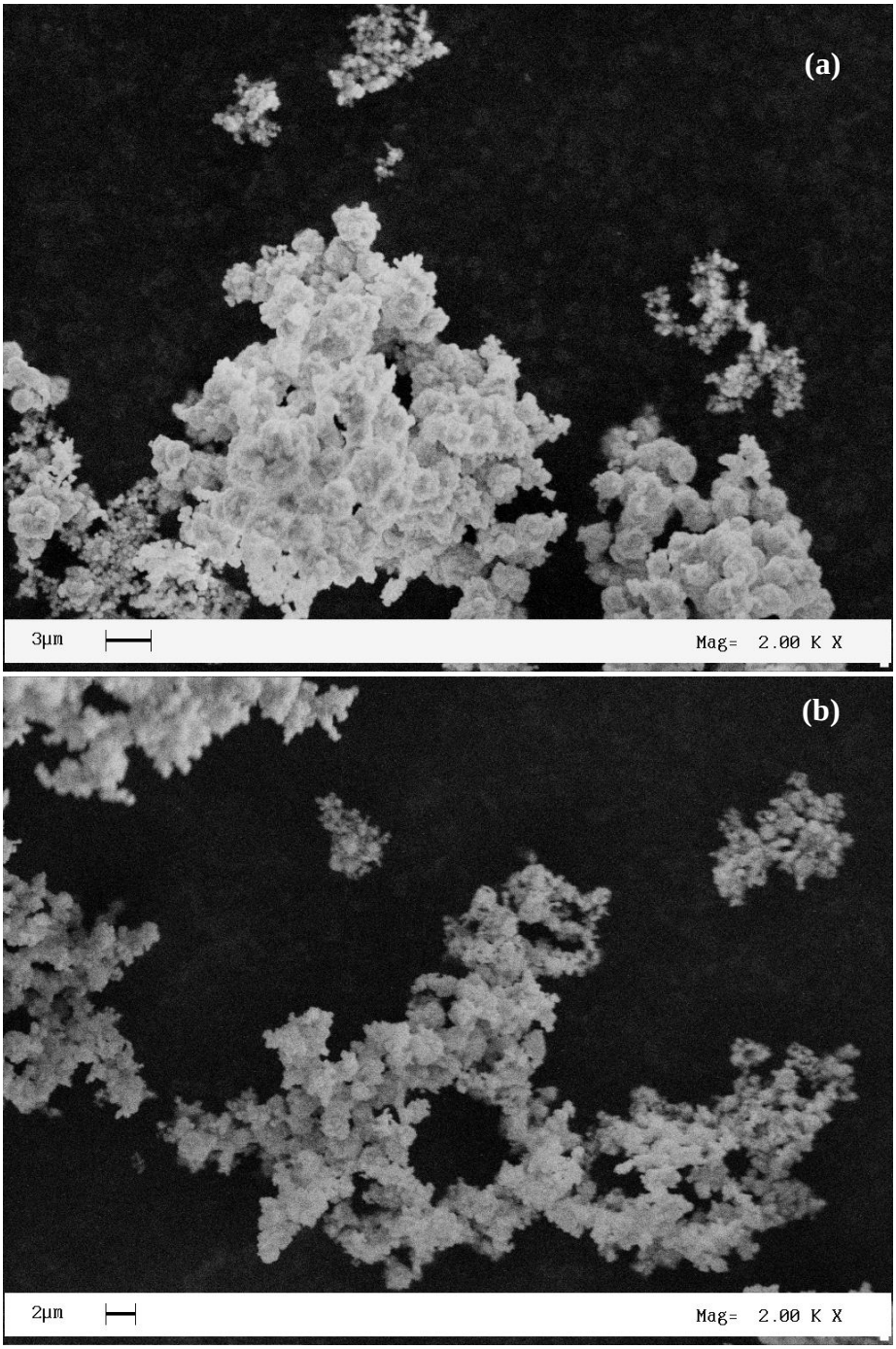

Fig. 5.5: SEM images for the samples with alanine: $n_{AgNO_3} / n_{C_3H_7NO_2} = 0.36$ (a) and $n_{AgNO_3} / n_{C_3H_7NO_2} = 0.18$ (b).

5.3 TEM characterization

For the sample with a double quantity of alanine, TEM analysis was also performed, using a FEI Tecnai 20 SUTW electron microscope operating at 200 keV. The image of Fig. 5.6, one of the first recorded at Salerno University, shows the presence of nanoparticles with dimensions in the range from 75 nm to 100 nm.

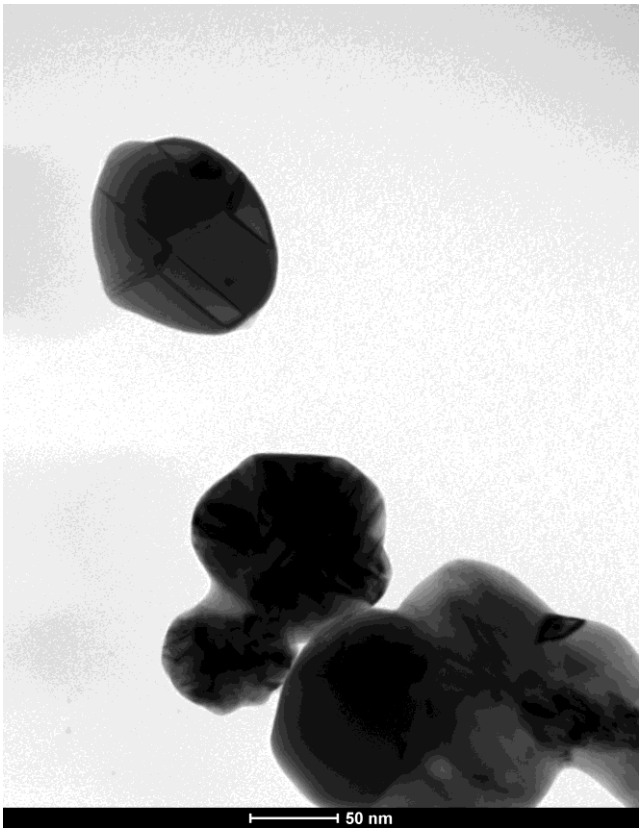

Fig. 5.6: TEM image for the sample with alanine $n_{AgNO_3} / n_{C_3H_7NO_2} = 0.18$.

5.4 Bibliography

[1] Regulla D.F., Deffner U. "Dosimetry by ESR spectroscopy of alanine". *International Journal of Applied of Radiation and Isotopes*, 33: 1101–1114, 1982.

[2] Funaro M., Di Bartolomeo A., Pelosi P., Saponetti M.S., Proto A. "A dosimeter based on silver-nanoparticle precursors for medical applications with linear response over a wide dynamic range". *Micro & Nano Letters*, 6(9): 759-762, 2011.

CONCLUSIONS

This dissertation collects the results of my own work on the development and implementation of new radiation dosimeters based on nanomaterials.

To get experience in the field of radiation dosimetry, conventional detectors were first used. In particular, Fricke detector, the father of chemical dosimeter, was developed and tested under gamma radiation, while radiochromic films were calibrated and their dosimetrical accuracy was compared with that of an ionization chambers 2D array.

Having in mind the simplicity of Fricke dosimeter, a liquid detector based on precursors of silver (Ag) nanoparticles was developed. The ionizing radiation induces the synthesis of Ag nanoparticles, as it is evident by the color change of the solution from transparent to yellow and by the presence of an absorption peak in UV-Vis spectra. The reading system of this detector is very simple. A linear response between the absorbance peak intensity characteristic of the Ag nanoparticles and the absorbed dose is obtained on a wide dynamic range, enabling a possible use of this detector both for Stereotactic treatments and conventional radiotherapy.

The response to radiation of other materials, such us silver nanoparticles, precursors of copper (Cu) nanoparticles, precursors of zinc sulphate (ZnS)

nanoparticles and manganese (Mn) doped ZnS nanoparticles, was also studied. Among these materials, only Mn doped ZnS nanoparticles show a physical variation after radiation, since their photoluminescence increases linearly with absorbed dose.

Both the detectors based on Ag nanoparticles precursors and Mn doped ZnS nanoparticles are relative dosimeters, since they require a calibration before being used. For this reason, these dosimeters, could find application for the evaluation of the dose distribution or dose verification but not for beam calibration. In order to construct an absolute dosimeter and overcome the limits of ionization chambers, real time radiation detectors with electrodes based on vertically aligned Multiwall Carbon Nanotubes (MWCNTs) and Graphene were developed and their charge collection efficiency was studied. It was found that their performance is superior than that of all the other tested ionization chambers (electrodes made both of conventional material and reference materials), at standard bias voltage. This allows to construct miniaturized radiation detectors. Moreover, MWCNTs based ionization chamber is able to collect charge also to zero volt, opening perspectives for in vivo applications.

As further research activity, a green approach to synthesize silver nanoparticles in alanine was proposed. This idea stems from the consideration that alanine dosimeters have been introduced on the market and by the successful application of silver nanoparticles precursors as radiation detector. This work can be considered preliminary for the construction of a silver/alanine nanocomposites based dosimeter.

The intimate nature of this thesis, which tracks a transversal path through the synthesis and application of nanomaterials in radiation dosimetry, is that of a seminal work for exploring new approaches to this discipline. I am a physicist and this experience has allowed me to widen my cultural luggage in fields different

from my own. Moreover, it was very exciting to finalize my research work with a real product, which has been the subject of a patent and of the Business Plans presented at Start Cup Campania, PNI and Nanochallenge 2012 competitions.

APPENDIX A

THE LINAC ACCELERATOR

A LINear ACcelerator (LINAC) is a radiation source and it is the device most commonly used for external beam radiation treatments for patients with cancer [1, 2]. The linear accelerator is used to treat all parts/organs of the body. It delivers a well-defined beam of uniformly intense x-ray photon radiation to the region of the patient's tumor. These x-ray treatments can be designed in such a way that they destroy the cancer cells while sparing the surrounding normal tissue. Most LINACs can emit x-ray photon radiation of different energy in the range form 4 MeV to 25 MeV.

The LINAC (Fig. A1) uses microwave technology to accelerate electrons and then allows these electrons to collide with a heavy metal target. As a result of the collisions, high-energy x-rays are produced from the target. These high energy x-rays are shaped as they exit the machine to conform to the shape of the patient's tumor and the customized beam is directed to the patient's tumor. The beam may be shaped either by blocks that are placed in the head of the machine or by a multileaf collimator that is incorporated into the head of the machine. The patient lies on a moveable treatment couch and lasers are used to make sure the patient is in the proper position. The treatment couch can move in many directions including up, down, right, left, in and out. The beam comes out of a part of the

accelerator called gantry, which can be rotated around the patient (Fig. A1). Radiation can be delivered to the tumor from any angle by rotating the gantry and moving the treatment couch. Instead to direct the electrons toward a metallic target producing x-ray photon radiation, some LINAC can use directly the produced electron beam as radiation source. In the head of the machine, it is decided if a monochromatic beam of electrons or photons has to be used. However, photon beams are most used in radiotherapy.

Fig. A1: ELEKTA LINAC

All accelerators have four major components: a modulator, an electron gun, a radio-frequency (RF) power source, and accelerator guide (Fig. A2) [2].

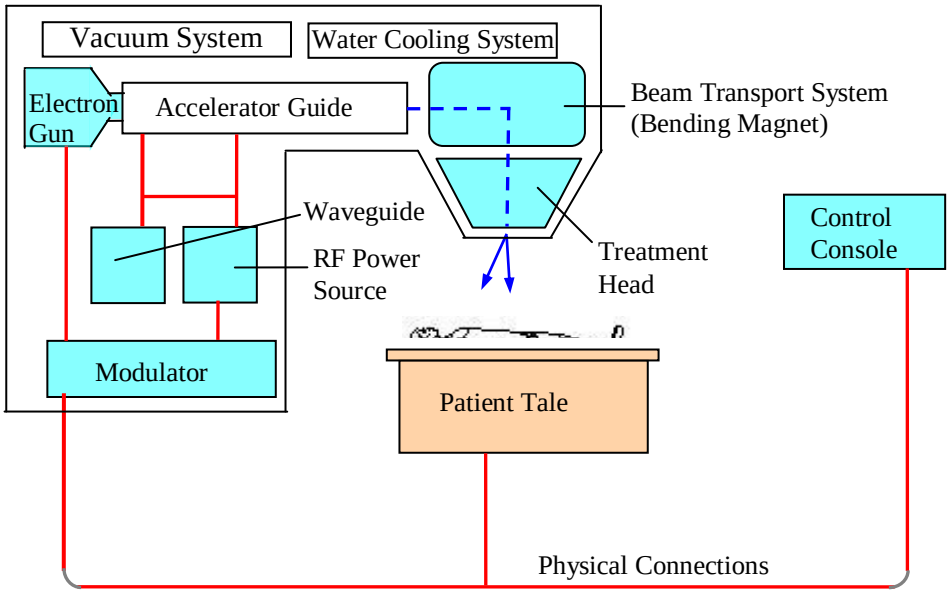

Fig. A2: typical LINAC components.

The modulator amplifies the AC power supply, rectifies it to DC power, and produces high-voltage DC pulses that are used to power the electron gun and RF power source. High-voltage cables electrically connect the electron gun and RF power source to the modulator, which can be located in the gantry, the gantry supporting stand, or a separate cabinet.

The electron gun is pulsed by the modulator and injects pulses of electrons of a few micro-seconds duration into the accelerator guide at energies of about 15-40 keV. The electrons are subsequently accelerated in the accelerator guide to the required energy level. The electron gun can either be a diode device with direct or indirect heating of the cathode, or a triode device in which the grid can be used to obtain control of the injected electron current in the electron mode.

The RF power source, either a magnetron or a klystron, supplies high-frequency electromagnetic waves (3000 MHz), which accelerate the electrons injected from the electron gun down the accelerator guide.

In practice, the accelerator guide is made up of a number of specially shaped, copper microwave resonant cavities that have been brazed together to form a single structure. Indeed, a charged particle traveling along the axis of a series of conducting tubes which are connected to an alternating voltage gets accelerated and acquires energy as it passes through each gap between the tubes. A system using a radio frequency supply was not found to be practical because the high velocity attained by the particles would require very long flight tubes when radio frequency was used. However, at microwave frequencies, it became possible to accelerate electrons to energies of several million electron volts. The length of the accelerator guide will vary from about 30 cm to 2.5 m, depending on the final electron energy and the type of structure utilized. Vacuum conditions need to be created in the accelerator wave guide so that the electrons being accelerated should not be deflected by collisions with gas atoms. For this purpose, an ion pump is used which has a working range of 10^{-3} to 10 torr.

Bibliography

[1] Greene D., Williams P.C. "Linear Accelerators for Radiotherapy". Taylor and Francis Group, 1997.

[2] Excerpt from a Healthcare Product Comparison System (HPCS) report from ECRI Institute entitled, Linear Accelerators; Radiotherapy Units, Cobalt, available at the web site

https://www.ecri.org/PatientSafety/Pages/Linear_Accelerators_Radiotherapy_Units_Cobalt.aspx

APPENDIX B

DOSE RELEASE TECHNIQUES IN RADIOTHERAPY

The two main divisions of Radiotherapy are External Beam Radiation Therapy (EBRT or XRT) and Internal Beam Radiation Therapy or Brachytherapy [1].

External-Beam Radiation Therapy is most often delivered in the form of x-rays photon beams. Patients usually receive external-beam radiation therapy in daily treatment sessions over the course of several weeks. The number of treatment sessions depends on many factors, including the total radiation dose that will be given.

The most common type of EBRT is called Conventional EXternal beam Radiation Therapy (2DXRT) and it is delivered via two-dimensional beams using linear accelerator machines. 2DXRT mainly consists of a single beam of radiation delivered to the patient from several directions: often front or back, and both sides. Conventional refers to the way the treatment is planned or simulated on a specially calibrated diagnostic x-ray machine known as a simulator because it recreates the linear accelerator actions, and to the usually well-established arrangements of the radiation beams to achieve a desired plan.

In the last decade, other methods of EBRT have been introduced in cancer treatment, such as Intensity Modulated Radiation Therapy (IMRT) and Stereotaxy.

Contrary to 2DXRT, IMRT is not based on uniform radiation fields but it utilizes beams by multileaf collimators [2, 3] that can be controlled during treatment, varying the radiation beam intensity across the targeted field. Because of this modulation an increased dose of radiation can be delivered to the tumor using IMRT. This technique has the capability of tailoring the isodose distributions closer to the tumor volume, thereby reducing normal tissue irradiation and potentially allowing dose escalation.

Stereotactic Radiosurgery (SRS) can deliver one or more high doses of radiation to a small tumor [4, 5], using extremely accurate image-guided tumor targeting and patient positioning. Therefore, a high dose of radiation can be given without excess damage to normal tissue. SRS can be used to treat only small tumors with well-defined edges. It is most commonly used in the treatment of brain or spinal tumors and brain metastases from other cancer types. SRS requires the use of a head frame or other device to immobilize the patient during treatment to ensure that the high dose of radiation is delivered accurately.

Stereotactic Body Radiation Therapy (SBRT) delivers radiation therapy in few sessions, using small radiation fields and high doses. By definition, SBRT treats tumors that lie outside the brain and spinal cord. SBRT can be used to treat only small, isolated tumors, including cancers in the lung and liver [5].

External-Beam Radiation Therapy can be performed also with electron beams instead of photon beams. However the treatments with electron beams are less frequent. They are useful for treating superficial lesions because the maximum of dose deposition occurs near the surface [6].

Internal radiation therapy (brachytherapy) is radiation delivered from radiation sources (radioactive materials) placed inside or on the body [7]. This technique is much less used than EBRT. The ratio between brachytherapy treatments and those performed with EBRT is above 5%.

In brachytherapy, radioactive isotopes are sealed in tiny pellets or "seeds." These seeds are placed in patients using delivery devices, such as needles, catheters, or some other type of carrier. As the isotopes decay naturally, they give off radiation that damages nearby cancer cells. If left in place, after a few weeks or months, the isotopes decay completely and no longer give off radiation. The seeds will not cause harm if they are left in the body (permanent brachytherapy).

Brachytherapy may be able to deliver higher doses of radiation to some cancers than external-beam radiation therapy while causing less damage to normal tissue [6 ,7]. It can be given as a low-dose –rate or a high-dose-rate treatment.

Bibliography

[1] Khan F.M. "The physics of radiation therapy", Lippincott Williams & Wilkins, 2003.

[2] Burman C., Chui C.S., Kutcher G. et al. "Planning, delivery, and quality assurance of intensity-modulated radiotherapy using dynamic multileaf collimator: a strategy for large-scale implementation for the treatment of carcinoma of the prostate". *Int. J. Radiat. Oncol. Biol. Phys.*, 39:863–873, 1997.

[3] Webb S. "The physical basis of IMRT and inverse planning". *Br. J. Radiol.* 76: 678–689, 2003.

[4] Noda S.E., Lautenschlaeger T., Siedow M.R., et al. "Technological advances in radiation oncology for central nervous system tumors". *Seminars in Radiation Oncology*, 19(3):179–186, 2009.

[5] Kavanagh B.D., Timmerman R.D. "Stereotactic radiosurgery and stereotactic body radiation therapy: An overview of technical considerations and clinical applications". *Hematology/Oncology Clinics of North America*; 20(1):87–95, 2006.

[6] Lawrence T.S., Ten Haken R.K., Giaccia A. "Principles of Radiation Oncology". In: DeVita V.T. Jr., Lawrence T.S., Rosenberg S.A., editors. *Cancer: Principles and Practice of Oncology* 8th ed. Philadelphia: Lippincott Williams and Wilkins, 2008.

[7] Patel R.R., Arthur D.W. "The emergence of advanced brachytherapy techniques for common malignancies". *Hematology/Oncology Clinics of North America*, 20(1):97–118; 2006.

APPENDIX C

EXECUTIVE SUMMARY NARRANDO

L'iniziativa imprenditoriale è volta alla soddisfazione di una significativa esigenza sociale quale la **riduzione degli errori di somministrazione** cui possono essere soggetti i pazienti sottoposti a radioterapia e radiologia. La letteratura scientifica e le linee guida internazionali evidenziano una sempre più sentita necessità, considerati i ricorrenti casi di incidenti e l'impiego di tecniche di somministrazione della dose sempre più sofisticate, del controllo della dose in vivo e, naturalmente, in *real time*, durante i trattamenti. Infatti, il malfunzionamento delle apparecchiature, il non corretto set-up del paziente, errori sistematici e occasionali possono vanificare l'accuratezza del trattamento oppure aumentare la tossicità delle radiazioni per gli organi critici (e.g. in radioterapia è necessario poter effettuare operazioni di correzione in continuo).

L'attività di NARRANDO (NAno caRbon RAdiatioN DOsimeter) è finalizzata allo **sviluppo**, **produzione** e **commercializzazione** di dosimetri nanostrutturati per la misurazione assoluta di dose in real time sia in ambito radioterapeutico, con applicazioni nella dosimetria in vivo, che nel settore radiologico, con prestazioni più elevate rispetto ai prodotti competitivi a costi significativamente più bassi. Per tali due mercati si realizzeranno camere a ionizzazione miniaturizzate, rispettivamente a base di nanotubi di carbonio e di grafene.

Il sostanziale **vantaggio competitivo** di questi prodotti, che li porrà sul mercato come innovazione radicale e, potenzialmente, *disruptive,* è il netto passaggio di scala che essi consentono. La miniaturizzazione, ottenuta grazie all'impiego delle nanotecnologie, permette infatti la misurazione della dose che un piccolo volume di materia assorbe durante un trattamento radioterapeutico con una elevatissima risoluzione spaziale, consentendo di effettuare misure in vivo o in distretti altrimenti impraticabili come il *bordo oculare* o applicazioni *brachiterapiche*. La miniaturizzazione risulta particolarmente utile anche in radiologia per misurare la dose in zone di piccola estensione, inaccessibili con i mezzi attuali. Inoltre, il **costo annuo equivalente** dei dosimetri nanostrutturati è inferiore a quello dei prodotti competitivi, mentre il margine di contribuzione è elevato, essendo i costi fissi e variabili relativamente bassi.

L'impresa si occuperà direttamente di tutte le attività, primarie e di supporto, connesse alla produzione e commercializzazione dei dispositivi, grazie al consolidato **know how** dei componenti del gruppo nel campo della fisica, della chimica e dell'ingegneria chimica applicate alla sintesi e alla caratterizzazione di nanomateriali, nonché alle competenze economico-manageriali. Inoltre, il team si avvale di un imprenditore che si occupa da anni della commercializzazione e manutenzione di dispositivi per la dosimetria in tutto il mondo.

Un **prototipo** del dosimetro è stato testato presso l'Unità di Radioterapia del Centro Polidiagnostico Check up di Salerno.

La strategia di **tutela** del concept e del prodotto fisico ha visto il deposito della domanda di brevetto *Dosimetro di radiazione "in tempo reale" basato su nanomateriali di carbonio* (SA 2012°000011 del 12/07/2012). Dal punto di vista gestionale, giocheranno ruolo indiscusso il prezzo competitivo e l'intensiva campagna di marketing volta alla fidelizzazione degli utilizzatori al brand, accompagnata dal lancio attraverso un pilot test presso un ristretto numero di

centri di eccellenza per la radioterapia e radiologia (tra le strutture disposte al lancio prodotto figurano l'Ospedale di Agropoli, Santa Maria di Terni, San Carlo di Potenza, Vito Fazzi di Lecce).

Tenendo conto delle statistiche IAEA (International Atomic Energy Agency), DIRAC (DIrectory of RAdiotherapy Centres), AIRO (Associazione Italiana di Radioterapia Oncologica), ESTRO (European Society for Radiotherapy and Oncology) ed ipotizzando che ogni anno venga acquistato 1 nuovo dosimetro "*duraturo*" in aggiunta o sostituzione ai precedenti per ogni sorgente di radiazioni (ipotesi peraltro estremamente cautelativa), è possibile affermare che il **mercato** mondiale della **radioterapia** richiederà mediamente 35.000 dosimetri nell'anno 2013. Il prodotto proposto, grazie alle elevate prestazioni e promesse e all'abbattimento delle barriere all'ingresso nella commercializzazione dei dispositivi (avendo, all'interno del team d'impresa, il proprietario di una ditta a ciò preposta), sarà un elemento destabilizzante per tali stime di domanda. Rispetto ai volumi conseguiti dal partner commerciale, si prevede di riuscire ad intercettare almeno il 2.3% di tale mercato mondiale (worst case, sul quale il business plan è tarato), sfruttando i contatti nazionali e internazionali preesistenti del team di impresa non solo con centri di terapia ma anche istituti di ricerca e università, per un volume di vendita per questo anno di circa 800 dispositivi. Negli anni successivi, all'aumento del numero di macchine per radioterapia (legato all'aumento di incidenza del numero di tumori) e grazie alla campagna di marketing e al word of mouth, il mercato intercettato subirà una notevole crescita. Non è inoltre da trascurare la possibilità di impiantare il dispositivo (e.g. in cavità naturali…) il che proietta il prodotto sul mercato estremamente più ampio degli usa e getta.

Rispetto al **mercato radiologico**, tenendo conto dei dati commerciali a disposizione del team (circa 30.000 dispositivi radiologici sul territorio nazionale

e 350.000 centri nel mondo, rapporto numero centri/numero dispositivi richiesti in un anno 1 a 1), in via del tutto cautelativa, si può ritenere di raggiungere, durante il primo anno di attività, un volume di vendita pari al 1600 unità, con un trend in crescita per i successivi anni.

L'idea di business risulta vincente per prestazioni e potenzialità applicative nettamente superiori rispetto ai prodotti competitivi; bassi costi sia fissi che variabili di produzione; margine di contribuzione elevato per entrambi i mercati (radioterapia e radiologia), con politica di *pricing* coerente con analisi costo annuo equivalente dei prodotti competitivi.

La tabella che segue mostra gli indicatori di sintesi nel caso di copertura degli investimenti con conferimento in capitale dei proponenti di €50.000,00 e finanziamento da parte di Venture Capital di €100.000,00. L'iniziativa risulta inoltre profittevole (tempo di ritorno dell'investimento di poco superiore ad un anno) anche nel caso di mutuo triennale.

DATI ECONOMICO/FINANZIARI SINTETICI (finanziamento Venture Capital)	1° ANNO	2° ANNO	3° ANNO
Fatturato	€ 648.000,00	€ 777.600,00	€ 933.120,00
EBITDA	€ 347.022,72	€ 460.132,32	€ 633.369,14
EBITDA/Fatturato	53,55%	59,17%	67,88%
EBIT	€ 290.264,20	€ 381.805,29	€ 537.473,58
EBIT/Fatturato	44,79%	49,10%	57,60%
Utile Netto	€ 172.064,61	€ 229.558,07	€ 327.456,44
ROI	60,12%	60,18%	53,72%
ROE	53,43%	41,62%	37,25%
Investimenti in Imm. Immateriali	€ 112.842,59	€ 104.842,59	€ 84.842,59
Investimenti in Imm. Materiali	€ 166.000,00	€ -	€ -
Equity (Capitale Sociale + Venture Capital)	€ 150.000,00		€ -